25

THE EFFECT OF MOLYBDENUM ON THE PROEUTECTOID FERRITE REACTION IN STEELS

THE EFFECT OF MOLYBDENUM ON THE PROEUTECTOID FERRITE REACTION IN STEELS

By

Robin B. Brown, B.E.Sc.

A. Thesis
Submitted to the Faculty of Graduate Studies
in Partial Fulfilment of the Requirements
for the Degree
Master of Engineering

McMaster University
August, 1979

Master of Engineering
Metallurgy

McMaster University
Hamilton, Ontario

TITLE: The Effect of Molybdenum on the Proeutectoid Ferrite Reaction in Steels

AUTHOR: Robin B. Brown, B.E.Sc. (University of Western Ontario)

SUPERVISOR: Professor G.R. Purdy

NUMBER OF PAGES: 113, ix

ABSTRACT

The effect of molybdenum on the isothermal proeutectoid ferrite reaction has been studied in low to medium (.05 - .43) carbon steels containing 1% molybdenum by weight. At 600 - 700°C molybdenum additions to steel result in the production of a dark etching ferrite constituent which has been shown to be heavily dislocated. The origin and stability of this transformation induced substrctures is considered.

In these alloys the austenite twin boundaries are sites for nucleation of ferrite. A simple model to describe nucleation on twins has been constructed and consequences for the equilibrium shape of a ferrite crystal in austenite developed. The equilibrium shape was determined experimentally and the shape is commensurate with the model developed.

ACKNOWLEDGMENTS

The author would like to thank all the people who made this thesis possible.

Foremost, I would like to thank my supervisor, Dr. G.R. Purdy, whose guidance and patience throughout the course of this work has been unending. Thanks also to Dr. J.D. Embury and the "rude mechanicals" for their encouragement when things didn't quite work out.

I am also grateful to the technical staff, whose valuable instruction made the experiments and this thesis possible. Thanks are due to Annette Neumayer and Susan Saracini for the fast and accurate typing of this thesis.

Finally, thanks to Gerry Moan, who said I should go to McMaster.

TABLE OF CONTENTS

Page

CHAPTER 1 INTRODUCTION AND LITERATURE REVIEW

CHAPTER 2 EXPERIMENTAL PROCEDURES

CHAPTER 3 EXPERIMENTAL RESULTS

CHAPTER 4 DISCUSSION

LIST OF TABLES

LIST OF FIGURES

CHAPTER 1

INTRODUCTION AND LITERATURE REVIEW

1.1 Introduction

The proeutectoid ferrite reaction has been studied by a number of previous workers and descriptions of the transformation products are well developed. The kinetic data for the transformations which occur in steel are generally illustrated in the form of Time Temperature Transformation (TTT) diagrams. The TTT curve for a plain carbon steel is shown in Fig. 1.1. The diagram shows that undercooling (cooling below the eutectoid temperature) is necessary for growth of a proeutectoid phase to occur and that by controlling the undercooling and time at that temperature, the microstructure can be controlled. The knee in the curve which occurs at approximately 550°C is a result of a maximum in the growth rate of pearlite. This knee in the curve is of considerable importance in relation to the heat treatment of commercial steels, because the kinetics of pearlite formation are so fast it would be very difficult to form structures which occur below the knee of the TTT diagram for thick sections of low alloy steels. Hence there would be finite limits on the strength and hardness which could be so obtained.

The role of alloying elements in steel is primarily to overcome this limitation, to suppress the formation of pearlite and to allow the formation of structures characteristic of greater undercooling. Most

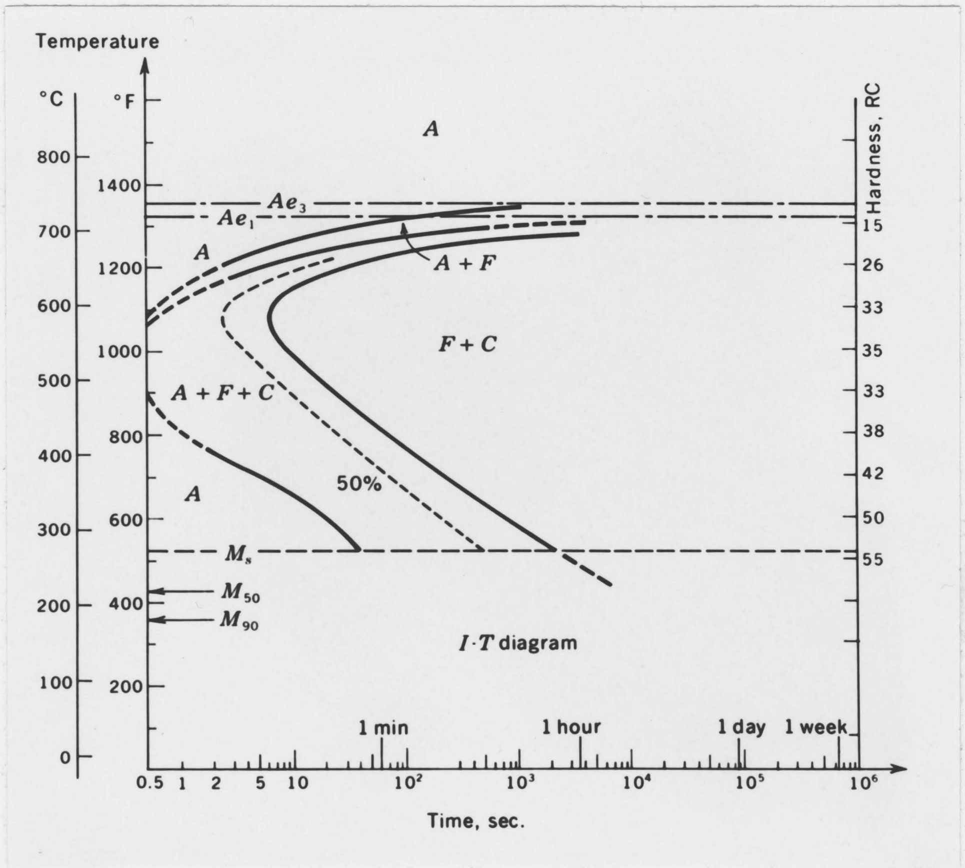

Fig. 1.1 TTT curve for a plain carbon steel (1060) (from Atlas of Isothermal Transformation Diagrams, USS).

alloying elements shift the curves to longer times as shown in Fig. 1.2 but elements such as molybdenum and chromium have a tendency to form a "bay" in the TTT diagram, Fig. 1.3. This bay separates two knees, one of which is for pearlite formation, the other for bainite formation.

Molybdenum is also useful in other respects, as a grain refiner, although its effect is not as pronounced as that of niobium or vanadium, Molybdenum can also precipitate as a number of different carbides, Theta (Mo_2C), Omega $(FeMo)C_6$, Kappa $(Fe,Mo)_{23}C_6$ and Cementite $(Fe,Mo)_3C$ which differ in composition,morphology and size.

Molybdenum in steels has been used to increase their toughness, to reduce the material's susceptibility to temper embrittlement and to prevent softening on tempering. It is also useful in obtaining a secondary hardening effect which makes molybdenum steels suitable for high temperature work where creep resistance is required.

The work carried out for this thesis was to further assess the effect of molybdenum on the proeutectoid ferrite reaction. The origin, stability and kinetics of the reaction products have been studied.

1.2 Literature Review

1.2.1 Fe-C System

1.2.1(a) Structure

The proeutectoid ferrite reaction product in the binary Fe-C system can be considered in terms of the morphologies developed in isothermal transformations. The shapes which develop upon transformation have been summarized into essentially six basic morphologies first by Dubé(1) and then modified by Heckel and Paxton(2). The modified Dubé system is shown in Fig. 1.4. The basic morphologies are:

1) Grain boundary allotriomorphs (Fig. 1.4(a)) - crystals nucleate

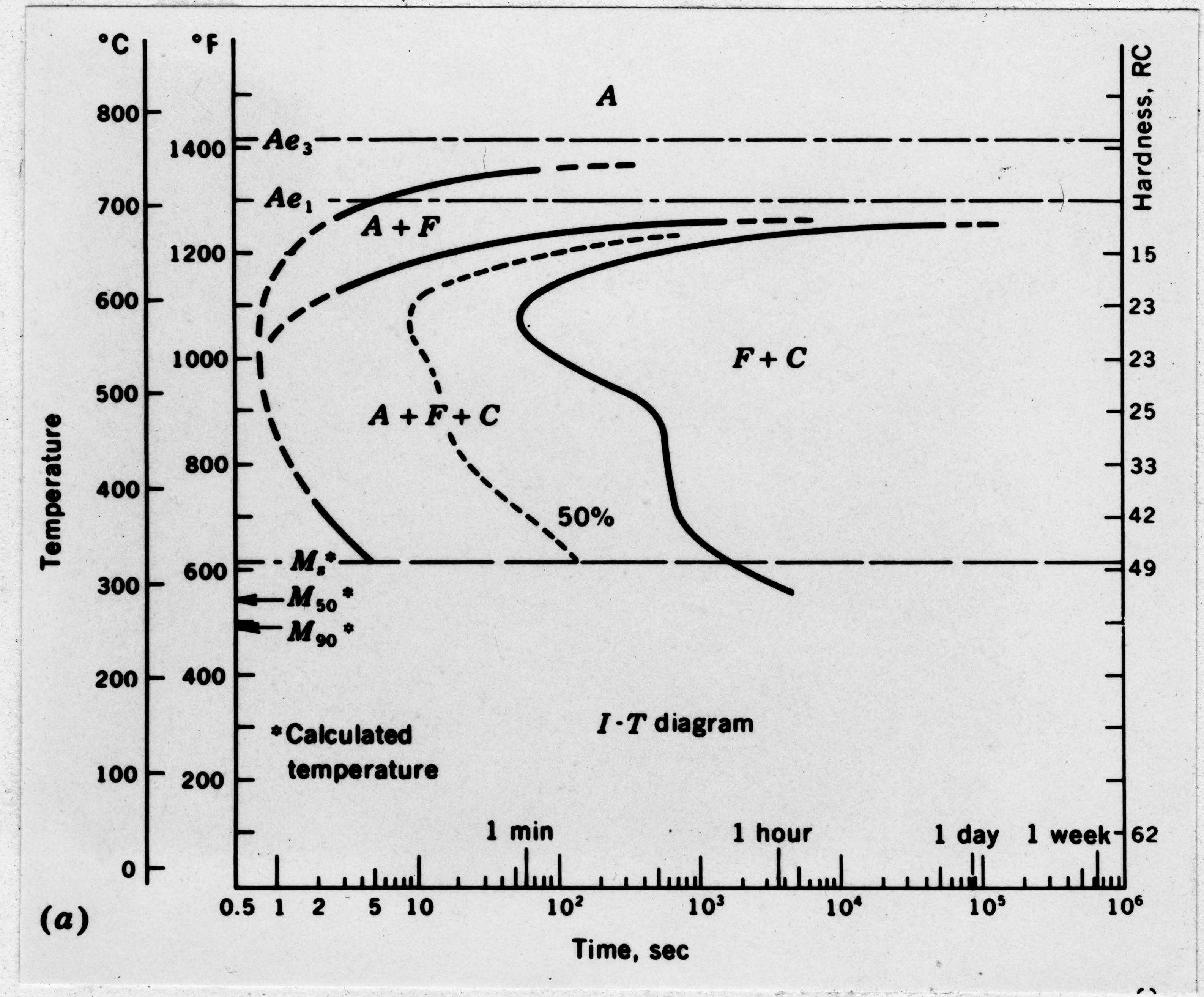

Fig. 1.2 TTT curves for alloyed steel. Note the shift of the nose to longer times. (from Atlas of Isothermal Transformation Diagrams, U.S.S.)

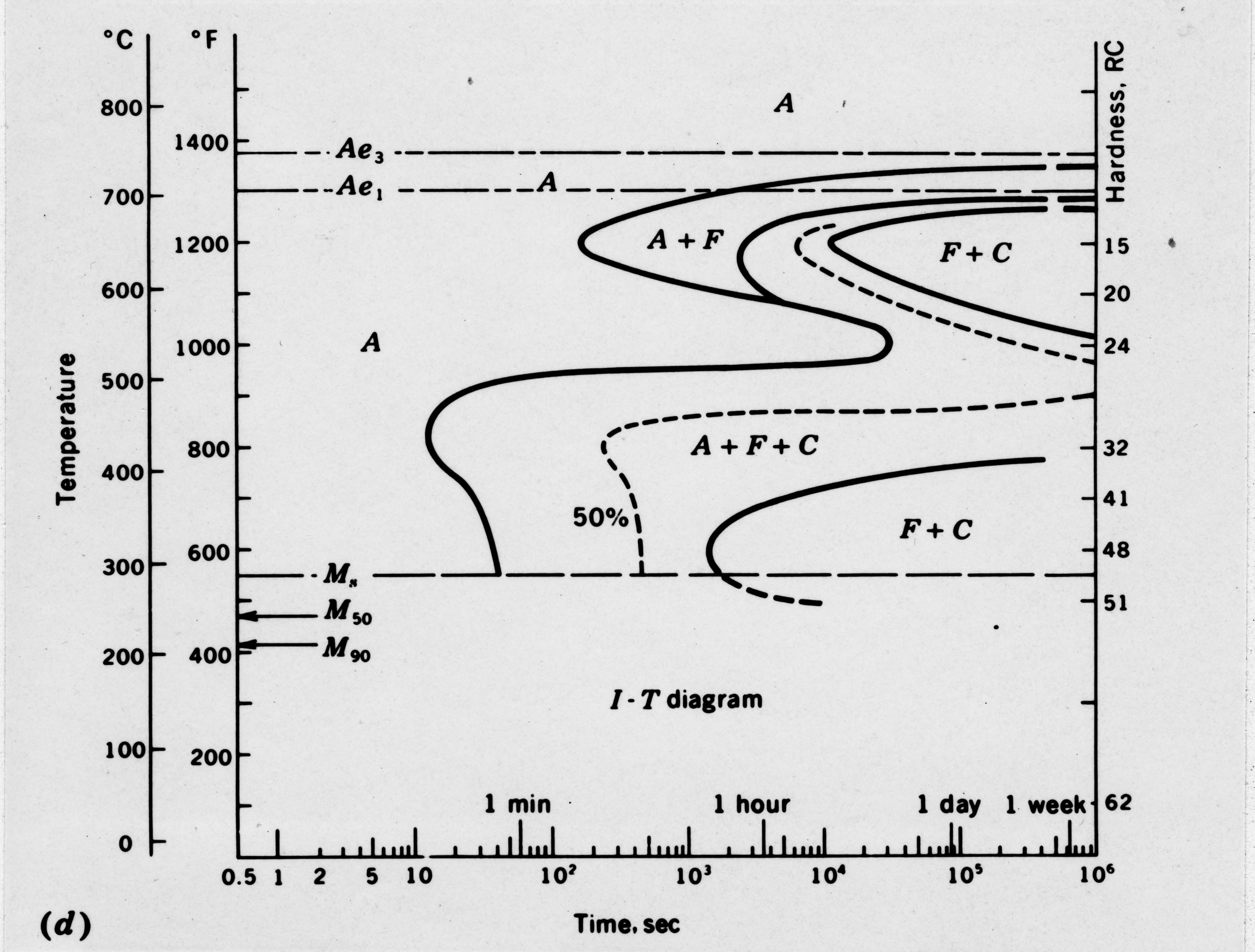

Fig. 1.3 TTT curve for Fe-C-Mo. Note the formation of a bay between 500° and 600°C. (from Atlas of Isothermal Transformation Diagrams, U.S.S.)

and grow along these boundaries.

2) Widmanstätten sideplates (Fig. 1.4(b)) - plates or needles which apparently nucleate at grain boundries and grow into the interior of the matrix grain. These sideplates can occur as primary (Fig. 1.4(b) (1)) or secondary (Fig. 1.4(b) (2)).

3) Widmanstätten sawteeth (Fig. 1.4(c)) - this morphology appears as a triangular cross section (as distinct from sideplates) in the plane of polish and occur as primary (Fig. 1.4(c) (1)) or secondary (Fig. 1.4(c) (2)) features.

4) Idiomorphs (Fig. 1.4(d)) - equiaxed cyrstals which form almost entirely in the interior of matrix grains.

5) Intragranular Widmanstätten plates (Fig. 1.4(e)) - formed in the interior of matrix grains.

6) Massive structure (Fig. 1.4(e)) - structure which results from the impingement of growing ferrite crystals.

The Dube classification is not only for the proeutectoid ferrite reaction. Other workers, Barrett et al.(3), Carter(4), Aaronson et al.(5), Mehl and Marzke(6) and Newkirk(7) have demonstrated that the same morphologies are developed in alloy systems where the "single phase precipitate forms in a single phase matrix by nucleation and diffusional growth"(8).

The first morphology to appear in hypoeutectoid steels is the grain boundary allotriomorph. After formation these grow along the boundaries until they impinge with other ferrite crystals. This process often continues until the grain boundaries are completely covered, after which the allotriomorphs will begin to thicken essentially as planar shapes. The allotriomorphs have been found to develop ragged or blocky interfaces on lowering the transformation temperatures to less than 700°C. Manning

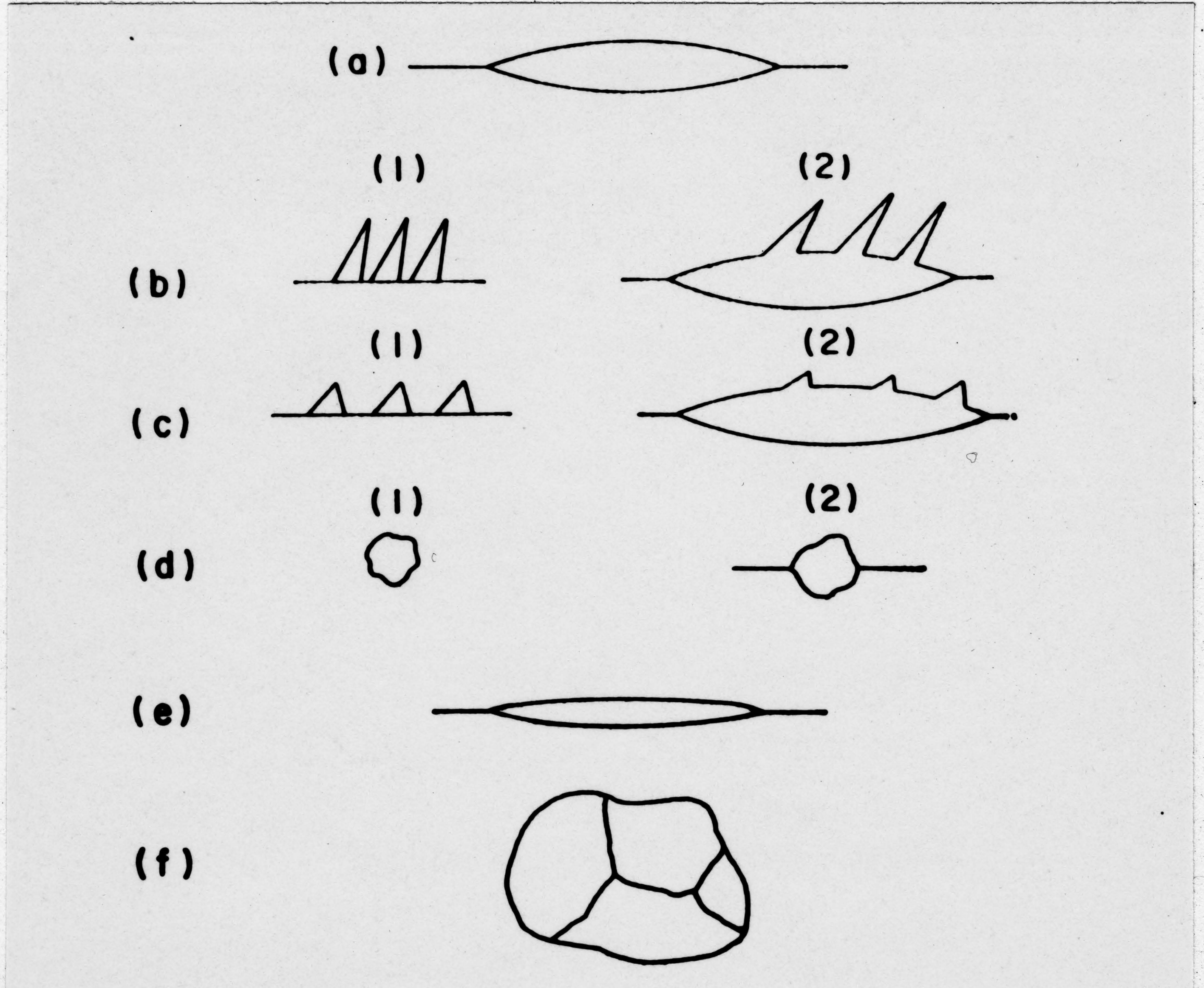

Fig. 1.4 The Dubé morphological classification system(1).

and Lorig(9) found this also true for alloy steels although at a somewhat higher temperature.

The thickening of allotriomorphs has been broken into two kinetic regimes; one involving primarily the influence of kinetic factors on the growth processes, and the second resulting in the minimization of interfacial free energy(8).

The growth or thickening of allotriomorphs is sometimes controlled by the volume diffusion of carbon in austenite. However, observations of faceting and of blocky structures indicates that the crystallographic nature of the interfaces are often important in terms of the migration kinetics. Two types of interfaces between ferrite (α) and austenite (γ) are considered to exist, one in which there is poor matching of atoms in the interface plane and the migration is "uncoordinated diffusion of individual atoms across the interphase boundary"(8). Inherent in this description is that these boundaries can migrate rapidly, the rate being controlled by factors such as concentration gradients, diffusivities and boundary curvature. The other type of boundary which can exist is one which has good lattice matching. These interfaces are generally made up of dislocation arrays interspersed with coherent regions; this type of structure has slow migration characteristics due to sessile components of the dislocation structure, slower than the disordered facets.

At high temperatures two factors are important in terms of formation of facets and blocky structure. Two driving forces are operative, the difference in chemical free energy of the precipitate and the matrix and the tendency to minimize the total interfacial free energy. The minimization of interfacial free energy is a very significant factor in the control of precipitate shape, especially at late stages as this process is still operative even when the chemical free energy difference has been reduced to zero. The driving force for interfacial free energy minimization is given by the Gibbs-Thompson equation (Eq. 1.1) which relates the concentration of the solute in the matrix C_1 in contact with a particle of radius of curvature r_1 and specific interfacial free energy σ_1 to the solute content of the matrix C_2 in contact with a particle of radius of curvature r_2 and specific interfacial free energy σ_2(8):

$$C_1/C_2 = \exp\ \{2\bar{v}/RT\}\ [\frac{\sigma_1}{r_1} - \frac{\sigma_2}{r_2}] \qquad (1.1)$$

$\bar{v}$ is the partial molar volume of solute in the matrix phase. This relation will determine which direction the concentration gradient will be set up, i.e., if $\sigma_1/r_1 > \sigma_2/r_2$ then $C_1 > C_2$ and the concentration gradient will cause particle 2 to grow at the expense of particle 1.

In terms of the two types of boundaries that exist, the coherent interface will have an infinite radius of curvature as it tends to be planar. Hence $(\sigma/r)_{\text{disordered}} > (\sigma/r)_{\text{dislocated}}$, resulting in dislocation or coherent facets expanding at the expense of the disordered or incoherent facets with a net decrease in the interfacial free energy of the system.

1.2.1(b) Nucleation Kinetics

The rate of nucleation of proeutectoid ferrite is generally expressed as the number of nuclei formed per second per unit area of unreacted grain boundary.

The basic requirement in the nucleation process is an expression for the concentration of critical size crystals of radius r^* at any time(10). The formation of subcritical crystals (embryos) requires an increase in the free energy and the mixing of these defects in the parent phase increases the entropy of the system. The number of embryos of radius r per unit volume C(r) can be related to the total number of atoms per unit volume (C_1), by:

$$C(r)/C_1 = \exp - \frac{\Delta G(r)}{kT}$$

This expression is limited by $r \overset{<}{\sim} a_0$ as $C(r)/C_1$ is not << 1 and the solution is no longer dilute.

It is also limited as r approaches r* (the critical radius) as the embryos become supercritical faster than they are produced.

The nucleation rate N_V is obtained by multiplying the concentration of critical embryos C* by the frequency (ν) at which an atom is added to a critical embryo, making it supercritical, where

$$N_V = \nu C^* = \nu C_1 \exp \frac{-\Delta G^*}{kT} \qquad (1.2)$$

$$C^* = C(r^*)$$

Eq. 1.2 indicates, in conjunction with Eq. 1.3, a pronounced dependence of N_V on ΔT and on $\gamma_{SL}{}^2$, the interfacial free energy. Fig. 1.5 illustrates the basic form of a free energy vs. radius, and the terms involved in making up the free energy terms, a volume free energy contribution $\Delta G_V \frac{4}{3}\pi r^3$ and the surface free energy term $\gamma_{SL}\, 4\pi r^2$. Also illustrated is the effect of increasing ΔT, which is to decrease the critical radius.

$$\Delta G^* = \frac{16\pi\gamma_{SL}{}^3}{3\Delta G_V{}^2} \propto \frac{\gamma_{SL}{}^3}{\Delta T^2} \qquad (1.3)$$

Several previous workers have focussed on obtaining these expressions more exactly for the proeutectoid ferrite case.

Mazanec and Cadek$^{(11)}$ collected data on a slowly reacting steel to obtain information representative of the general case. They found that N_V initially increases with time and then decreases. Their data are

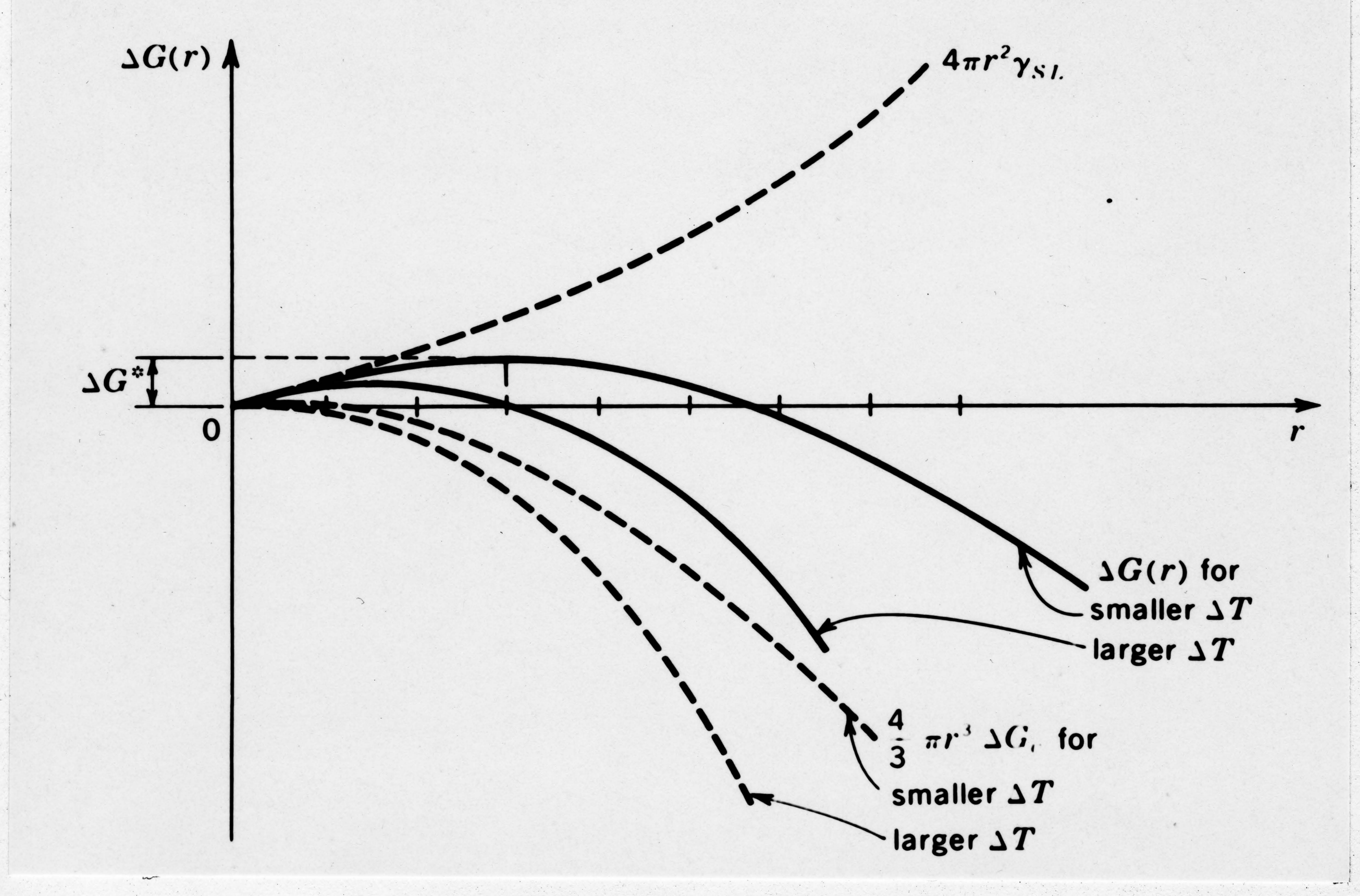

Fig. 1.5 Free energy versus radius as a function of undercooling (ΔT). Surface and volume free energy terms are also plotted as a function of undercooling. (Shewmon(52),p.159)

presented in Fig. 1.6. The rate of nucleation was found to follow a relationship of the form:

$$N_V = \alpha[1 - \exp \beta(t - \tau)] \qquad (1.4)$$

when N was increasing, and:

$$N_V = C/t^{1/2} \qquad (1.5)$$

when N_V was decreasing. Further experimentation on nucleation rates revealed that N_V increases rapidly with decreasing transformation temperature and that decreasing the austenitizing temperature from 1100°C to 950°C decreased N_V.

Some similar work was completed by Hickley and Woodhead(12) on plain carbon with low alloy additions. They too found that the rate of nucleation increased rapidly with decreasing temperature and carbon content.

1.2.1(c) Growth Rates

The growth rates of the supercritical embryos which nucleate are determined by the morphology of the embryo which in turn dictates the mechanism of growth.

The conventional approach to the problem of ferrite growth, is one which is determined by the long-range diffusion of carbon in the austenite instead of the transfer of iron atoms across the interface. However, there is a certain variation of growth rates which can be obtained in ferrite growth under given conditions. This is easily shown when a ferrite crystal grows into one grain faster than into an adjacent grain, which implies that the mobility of the ferrite austenite interface is a factor in determining the growth kinetics. The combination of interface mobility and carbon diffusion serves to complicate the mechanism of ferrite growth.

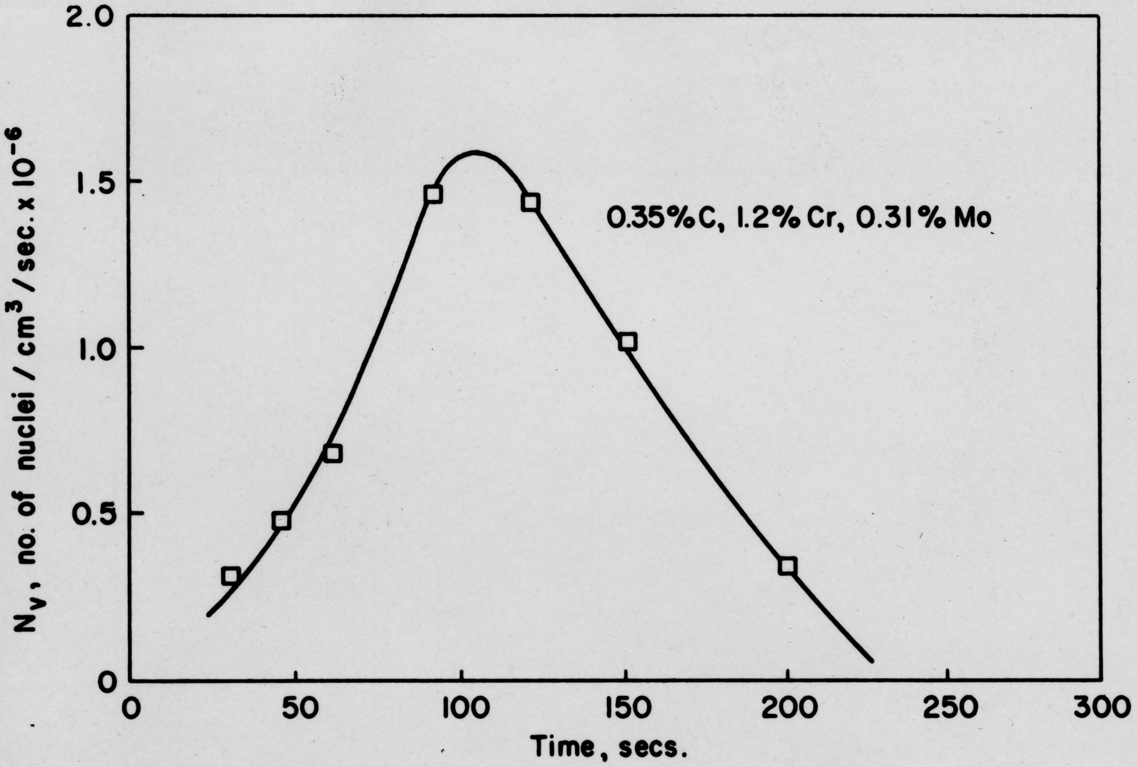

Fig. 1.6 Plot of nucleation rate N_V versus time. (Mazanec and Cadek[(11)]).

Zener(13) used a simple approach in which he assumed that the diffusion of carbon in austenite is the controlling step, to give an upper limit on the growth rate. By assuming that equilibrium exists at the α/γ interface, compositions can be read from the Fe-C phase diagram and a plot percentage C versus distance from the interface can be plotted as in Fig. 1.7. This plot illustrates that for the interface to advance a distance dx the solute must be removed from the volume transformed. This can only occur by diffusion. The amount of solute which must be removed, $dx(C^\gamma - C^\alpha)$ is equal to the flux, J_i, times the corresponding time increment dt. From this Zener obtained the following expression:

$$\frac{dx}{dt} = V = \frac{-J_i}{(C^\gamma - C^\alpha)} = \frac{D}{(C^\gamma - C^\alpha)} \frac{\partial C}{\partial x}$$

which relates this information to the velocity of the interface. Since carbon must be conserved in the process, the shaded areas of Fig. 1.7 must be equal; on continued precipitation of x the carbon gradient in the austenite will continue to decrease continuously. Using a simple linear estimation (the Zener approximation) the effective diffusion distance L can be calculated:

$$\left(\frac{\partial C}{\partial x}\right)_{x=\xi} = \frac{C^\gamma - C_0}{L} \qquad (1.6)$$

At increasing time $C^\gamma - C_0$ remains constant and L increases with time, "roughly" equal to $\sqrt{Dt}$. Hence, he finds the velocity proportional to $t^{1/2}$.

Bradley et al.(14), found that for grain boundary allotriomorphs, the thickening and lengthening kinetics followed a parabolic relationship, i.e.:

$$S/2 = \alpha t^{1/2}$$

$$L/2 = \beta t^{1/2}$$

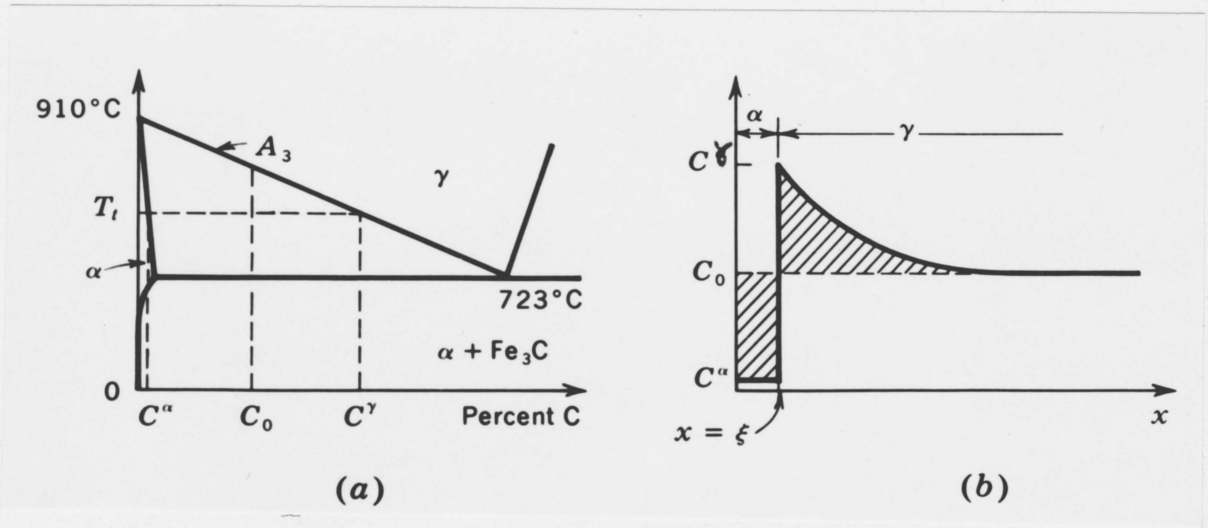

Fig. 1.7 (a) Fe-C phase diagram and (b) the carbon concentration normal to the α/γ interface. (Shewmon(52), p.217)

where S is the thickness and L the length of the allotriomorphs. The constants α and β were found to increase with decreasing reaction temperature.

The mechanism of Widmanstätten evolution was modelled by Townsend and Kirkaldy(15). A ferrite crystal (Fig. 1.8(a)) which has nucleated on a γ boundary and has formed a Kurdjumov-Sachs(16) relationship with one austenite grain and an irrational relationship with the other. The nucleus grows along the boundary until a curvature in the boundary is encountered (Fig. 1.8(b)). The result of the curvature is to create surface anisotropy which would cause the distortion shown in Fig. 1.8(c).

The equilibrium shape will be overshot due to enhancement of the diffusion field and simultaneously send out side bands as theoretically described by Sekerka(17), Figs. 1.8 (d) and (e). The side bands will reach an amplitude at which its right-hand side will attain epitaxy with the austenite and it will then undergo a distortion due to anisotropy which is amplified by the diffusion field into a Widmanstätten plate.

1.2.1(d) Theory of Plate Formation

The formation of plate morphologies is a result of several mechanisms operating coincidentally.

Mehl and Barrett(18) proposed the formation of intragranular plates be due to point effect diffusion at the edges of the plate shaped nucleus, the resultant concentration gradients providing the driving force for rapid growth. However, this mechanism cannot account for the crystallographic homogeneity, i.e., evolution of side plates on only one side of four habit planes, that occurs in these crystals.

Nabarro(19) developed a theory based on strain energy minimization. Assuming that the precipitate crystal behaved as an incompressible inclu-

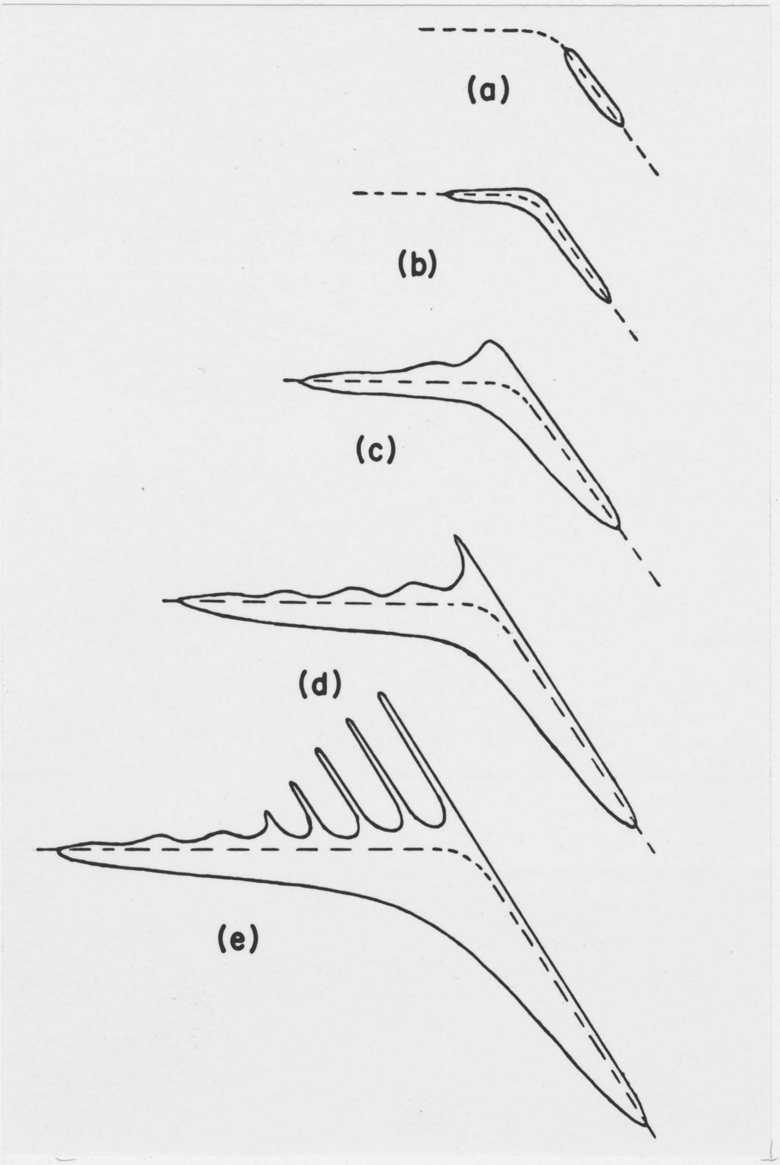

Fig. 1.8 Profile of developing Widmanstätten plates. (Townsend and Kirkaldy(15)).

sion, enclosed by a disordered boundary, the volume strain energy would be taken up by the matrix. A plot of strain energy (W) vs. shape of crystal C/a, Fig. 1.9 indicates that the strain energy can be reduced by the precipitate forming in flat sheets. This is true provided the precipitate is not coherent with the matrix. If it is, there will be an appreciably smaller reduction in the volume free energy. Nabarro still failed to account for known crystallographic relationship between the matrix and the precipitate. The good matching of planes (K - S relationship) $\{111\}_\gamma$ and $\{110\}_\alpha$ with best matching along conjugate directions $[\bar{1}10]_\gamma$ and $[111]_\alpha$ are not favorable since the shear modulus is at minimum in the <111> directions in both lattices and of intermediate value in <110> direction.

Nabarro concluded that a precipitate crystal bounded at all orientations by an incoherent interphase boundary provided the best opportunity for plate formation.

The final prediction was that plates predominate at low undercoolings and idiomorphic crystals at high undercoolings. This dependence on reaction temperature is completely opposite to the observed reactions in this system and in others(20).

Laszlo(22-26), in an attempt to account for the predominant morphology in terms of volume strain energy minimization found that for:

$$W = 6\ \mu\nu\lambda^2\ f(C/a) \tag{1.6}$$

where μ is the modulus of rigidity, ν the volume of precipitate crystal and λ the linear misfit, that:

$$W_{plate} < W_{cylinder} < W_{sphere}$$

However, the same basic criticism of Nabarro is applicable to this account, that interfacial energy and structure are more significant than the strain energy contribution in the formation of plates.

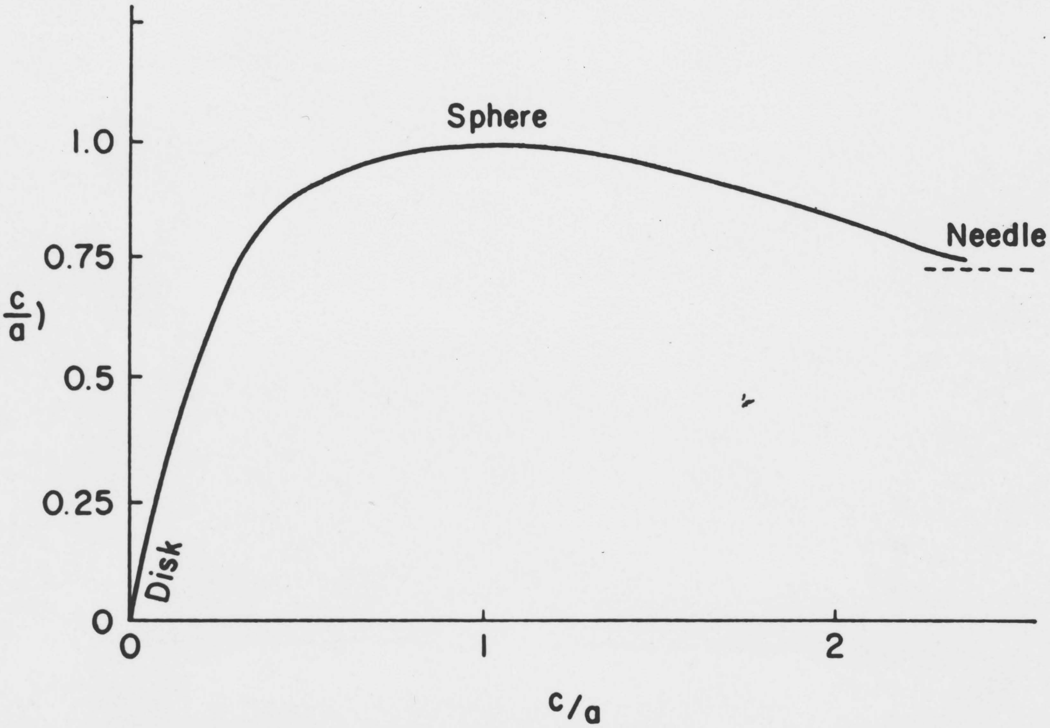

Fig. 1.9 Plot of volume strain energy W as a function of C/a, the semi-axial lengths of a precipitate crystal. (Nabarro$^{(19)}$)

C.S. Smith(27) proposed a theory based on the interfacial structure and energy of the resultant morphology.

Incoherent boundaries are considered isotropic and permit rapid diffusion along them. These boundaries are extremely mobile, a result of point effect diffusion.

Semi-coherent boundaries are constructed of dislocations, uniformly spaced. These arrays develop some volume strain energy which accounts for the decreased mobility of this boundary.

Coherent boundaries have no dislocations yet contain substantial amounts of volume strain energy which ultimately causes the lack of mobility of these interfaces.

Undercooling below the equilibrium temperature and the nature of the interface provide an adequate description of the morphology of the precipitate. At low undercooling, coherent growth requires more than the available volume free energy to overcome the volume strain energy for growth to occur. Whereas at large amounts of undercooling the volume free energy is large enough to support growth of coherent interfaces, hence a theory which can account for Widmanstätten formation and growth.

Kinsman, Eichen and Aaronson(28) in some studies on thickening kinetics of proeutectoid ferrite plates found that thickening was not controlled by volume diffusion of carbon in austenite. They suggested that a barrier to growth existed at the broad faces of the ferrite plates and that the structure of these was not of a disordered nature. Based on a theoretical study by Jones and Trivedi(21) of ledge growth, Kinsman et al. described the behavior of proeutectoid plates similarly when the plate spacing was small and the diffusion fields of adjacent ledges did not overlap. This treatment requires a growth rate less than that allowed by diffusion control, which was obtained in the experiments by Kinsman et al.

A schematic illustration of the evaluation of ledges is shown in Fig. 1.10. The ledges could evolve from curved portions of the interface that approach the broad faces by breaking into partially coherent segments (Fig. 1.10(a)) or as a result of plastic deformation due to the volume change from austenite to ferrite (Fig. 1.10(b)). The ledges were most likely a result of the emmission of a few dislocations from the broad faces into either phase from a given position along the boundary. The dislocations being readily nucleated under the driving force of the volume strain energy which accompanied the transformation.

Other mechanisms proposed were the characteristic irregularity of the broad faces of the ferrite sideplates which could serve as a source of ledges (Figs. 1.10(c) and (d)).

1.2.1(e) Equilibrium Shape

Hoffman and Cahn(29) proposed a vector formulation for the influence of excess surface free energy γ on the shape of physical surfaces. The scalar quantity $\gamma(\hat{n})$, an empirical thermodynamic function of surface orientation only, with $\hat{n}$ the unit vector normal to the surface and that $\int \gamma dA$ is the reversible work to create the surface. Equilibrium shapes are determined by minimizing the integral within the constraints of the system. The vector function $\xi(\hat{n})$ is chosen such that its component on the unit normal $\hat{n}$ represents the tendency for the surface to minimize free energy by contraction, where ξ, the component off the normal represents the tendency of the surface to minimize the free energy by rotation. The tensile and torque components of the thermodynamic force to be balanced

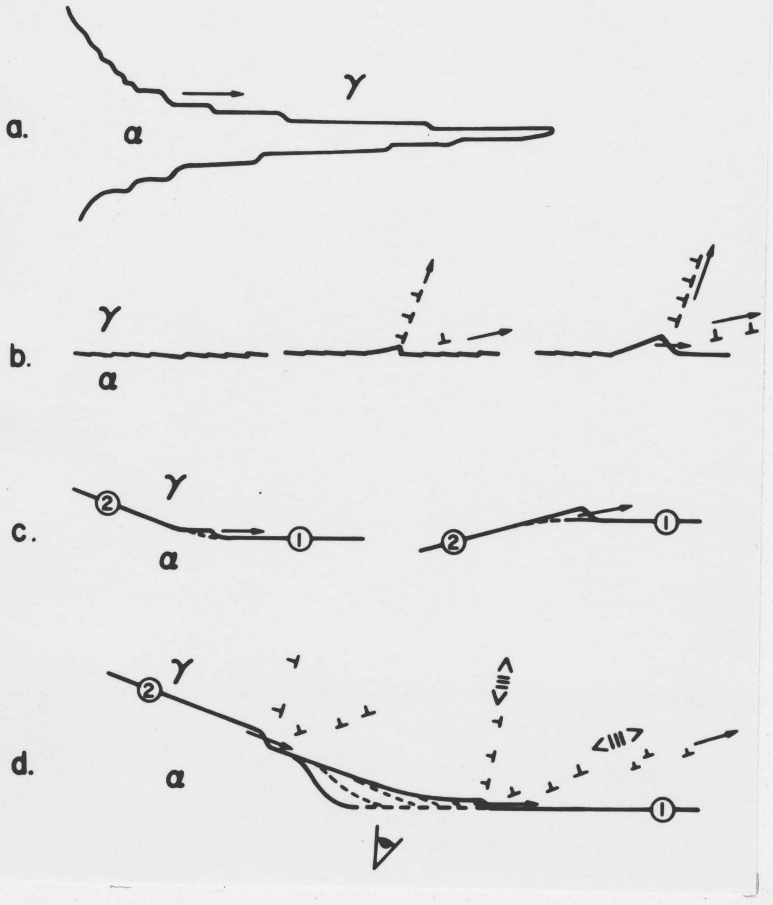

Fig. 1.10 Sources of ledges.
(Kinsman et al.$^{(28)}$)

at any exposed edge of a planar surface can be obtained by elementary methods. The ξ vectors are in fact radius vectors of the corresponding Gibbs-Wulff form for the shape of the equilibrium body.

1.2.1(f) Effect of Alloy Elements

The common use of alloying elements in steel is to slow down the transformation kinetics, graphically illustrated by shifting the TTT curve to the right, i.e., to longer times. Many of these additions serve to control the nucleation and growth of pearlite and bainite.

Shewmon(30) describes the effect of alloy elements as follows. If the element was distributed homogeneously in the austenite, the alloying element, after transformation will be partitioned to either the carbide or the ferrite phase. This process requires the substitutional element (alloy) to diffuse, which is generally slow at transformation temperatures. If the alloy element is not partitioned but is still homogeneously distributed between the ferrite and carbide phases, the structure is either metastable or unstable. Fig. 1.11 shows the partitioned and the unpartitioned effect on the binary phase diagram. At temperatures below A_1 and above $T_{eut.}$ the austenite will decompose into partitioned ferrite and carbide. This transformation rate is controlled by the diffusion of the substitutional alloy element. If the transformation occurs below $T_{eut.}$, the austenite will decompose into unpartitioned ferrite and carbide in which the alloy element is homogeneously distributed, the free energy change ΔG_V being markedly reduced in the latter case.

The reduction in transformation can be related to a number of factors: the free energy barrier to nucleation, the types of interfaces developed in the precipitates, and their relative energies.

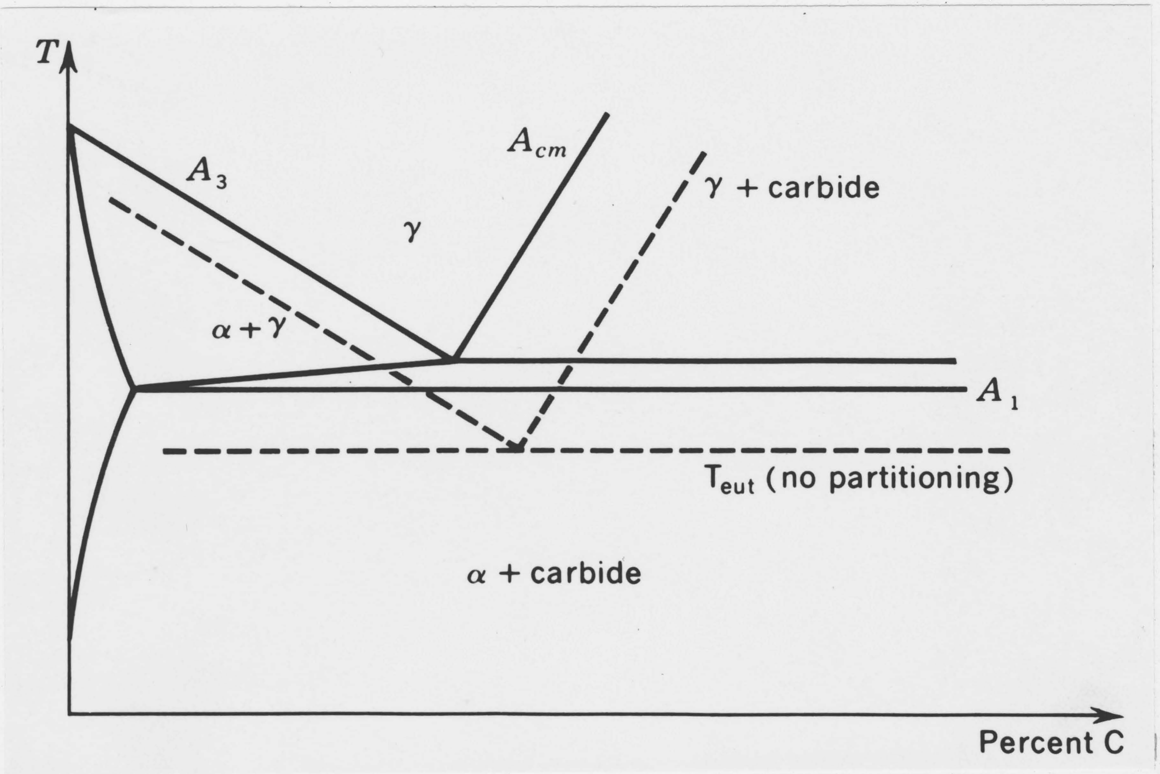

Fig. 1.11 Schematic phase diagram for an Fe-C-X (X is a substitutional solute). Between solid and dashed lines precipitation can only occur in the austenite if X is partitioned between the phases. (Shewmon$^{(52)}$, p.248)

The effect of alloying elements on the growth of ferrite has been treated in a review paper by Purdy(31). One approach to the problem is to extend the local equilibrium model to ternary systems in which the two solutes diffuse at vastly different rates. Coates(32) illustrated the concept of an alloying element spike at the phase boundary by solving the multicomponent diffusion equation(33) for the semi-infinite local equilibrium boundary condition. As the ratio of solute diffusivities increases, two regimes appear on the phase diagram, one in which the velocity is fast and is determined by the diffusion of the faster component, and a region in which the velocity is slow and controlled by the diffusion of the slow component. The line dividing these regions is known as the "envelope of zero partition" after Purdy et al.(34). This line is a result of partitioning or lack of it, of the slow diffusing solute in regions of low and high supersaturation respectively. This is shown in Fig. 1.12 (after Purdy et al.(31)). When the ratio of diffusivities is 10^4 or more, the kinetic boundary separating regions of fast and slow growth can be plotted onto a ternary isotherm.

When alloying elements cannot partition on the local equilibrium model and growth is determined by diffusion of carbon, different results are obtained from local equilibrium and paraequilibrium analyses.

This is a result of interfacial carbon potentials of parent and product phases differing between true and paraequilibrium, even though the carbon activity is assumed to slowly carry through the interface in both models.

In a recent review, Honeycombe(35) has shown that alloying elements greatly influence the type of carbide morphology encountered during direct transformation of austenite. This is achieved in two basic ways:

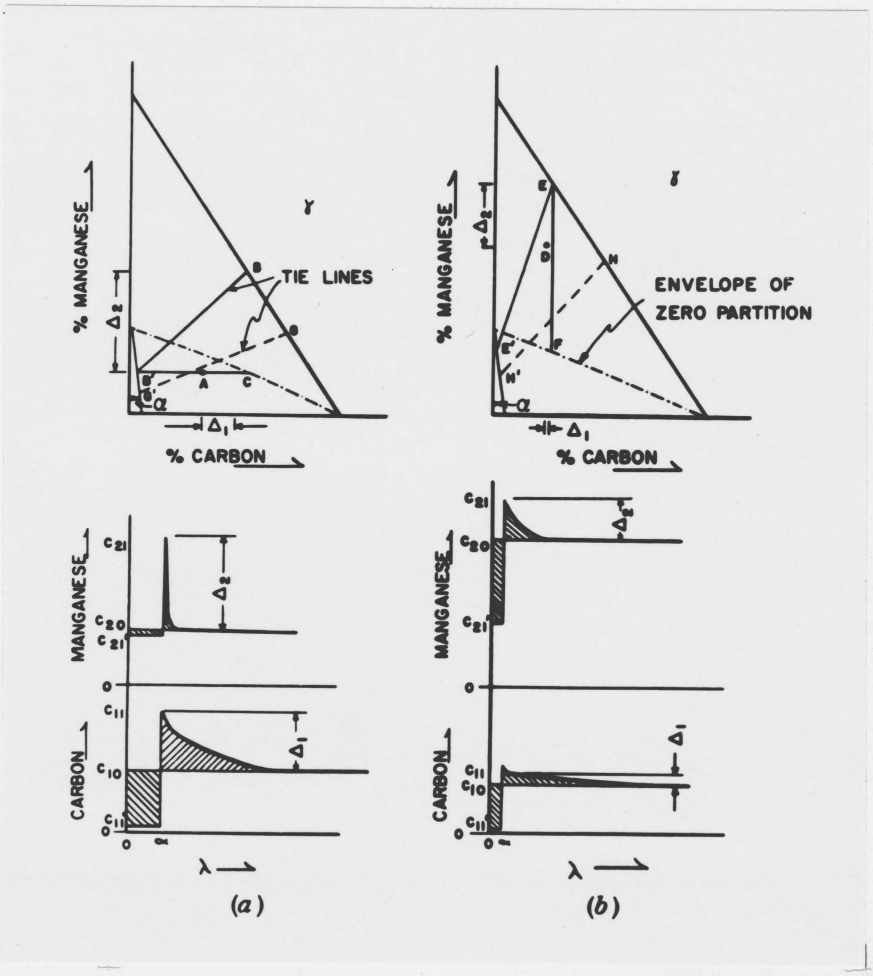

Fig. 1.12 Schematic penetration curves in X space for ferrite growth in Fe-C-Mn austenites. Mass balances are indicated by equal shaded areas on either side of the interface. Interfacial concentration given by tie lines B - B' and E - E'. (after Purdy et al.$^{(34)}$)

1) by altering the kinetics of the γ/α reaction, and

2) by changing the composition and structure of the carbide phase.

Slowly transforming steels tend to favor fibrous carbide growth, which represents a closer approach to equilibrium than the energy demanding process of repeated nucleation of particles at the γ/α interface.

However, some alloy elements do not obey this behaviour, tungsten in steels being one example. In this case the interphase precipitation of $(FeW)_6C$ (a complex cubic carbide) predominated, not the W_2C which is isomorphous with hexagonal Mo_2C. The conclusion to be drawn from this is that crystallogrphic factors influence the growth as well as the kinetic factors. Data from Davenport et al., Harding and Dyson et al. on lattice mismatch (Table 1.1) indicates that favorable orientations and structures exist in light of the mismatch which exists.

For example, the preponderence of Mo_2C fibres is probably due to the low degree of misfit in only one direction, whereas for VC two directions of low misfit result in a plate-like habit.

1.2.2 The Fe-C-Mo System

1.2.2(a) Structure

The initial work on the effect of molybdenum on the transformation characteristics of hyopeutectoid steels was carried out by Hultgren et al.(36). Hultgren found that the structure of the proeutectoid ferrite constituent which formed varied with the temperature of formation. The ferrite formed at high transformation temperatures, 700°C was found to be smooth etching with a reasonably smooth interface with the austenite. At transformation temperature below 675°C, the proeutectoid constituent was found (after suitable etching), to have a wrinkled surface appearance and a jagged interface with the austenite. Hultgren found these two

Table 1.1 Lattice mismatch for vanadium and molybdenum carbides in ferrite and austenite. (Honeycombe, R.W.K., Met. Trans., 7A, (1976), p.925)

	VC		Mo_2C	
Matrix	Orientation Relationship	Misfit,Pct	Orientation Relationship	Misfit,Pct
α	$[100]_c//[1\bar{1}0]_\alpha$	2.6	$(00.1)_c//(011)_\alpha$	16.5
	$[010]_c//[110]_\alpha$	2.6	$(01.0)_c//(01\bar{1})_\alpha$	28.3
	$(001)_c//(001)_\alpha$	45.2	$(2\bar{1}.0)_c//(100)_\alpha$	4.7
γ	cube/cube	16.0 all directions	$(00.1)_c//(111)_\gamma$	14.1
			$(11.0)_c//(1\bar{1}0)_\gamma$	18.4
			$(1\bar{1}.0)_c//(11\bar{2})_\gamma$	- 11.2

features became more pronounced as the transformation temperature is lowered and less pronounced on increased holding time at temperature. This microstructure is characteristic of molybdenum-containing steels and has also been found to occur in chromium, tungsten and vanadium steels.

Pitsch and Schrader(37), Berry and Honeycombe(38,39) and Purdy(40) have substantiated the initial findings of Hultgren and as well proposed some mechanisms which might account for the formation of the wrinkled constituent.

Hultgren found the wrinkles developed with some regularity and that the transformation from ordinary to wrinkled ferrite occurred gradually. He considered that it was the same type of ferrite (orthoferrite), which is formed continuously along the transformation and the production of wrinkled ferrite was an orthoreaction which occurred over a certain temperature range. In Hultgren's notation "ortho" means "partitioned". Recent work has disproved this idea.

Pitsch and Schrader(37) using transmission electron microscopy were able to determine the cause of the etch relief of the wrinkled ferrite: a very fine geometric cell structure with dimension of the order of 1000 Å. The existence of the cell structure was thought to be due to disturbances in the ferrite lattice which is contained in the cell walls. They felt that it was not possible for the lattice disturbance to be caused by a change in the molybdenum concentration as put forward by Hultgren et al.(36). This was tested by measuring the effect of molybdenum on the ferrite lattice constant, and it was found that the change was not significant(37). Research on the cold rolling of pure iron resulted in microstructures which were similar to those of the molybdenum steels. The homogeneous cell structure which resulted from plastic deformation was also found when the Mo steel was cold rolled; hence, they were not able to explain why only Mo steels produce wrinkled ferrite on transformation.

The work by Honeycombe(38,39), Berry(38) and Purdy(40) was focussed less on the deformation mechanism of cell formation, but on the interaction of interfaces with carbide dispersions.

Work by Purdy(40) on the wrinkled ferrite indicated that the dislocation density increased with decreasing temperature as was found by Pitsch and Schrader(37). He found that the transformation product formed at lower transformation temperatures much faster than the rate of long-range diffusion. He speculates that the wrinkled ferrite is a carbide/ferrite mixture which forms under greater degrees of departure from local $\alpha - \gamma$ equilibrium as the supersaturation is increased. This was found to be consistent with his observation of carbides which had been precipitated along the dislocations. He suggests that carbide formation be prerequisite for the growth of dislocated (wrinkled) ferrite, based on the observation that similar dislocation structures are produced in the wake of grain boundaries in ferrite which are forced through arrays of finely dispersed precipitates.

Bäro and Perepezko(41) observed dislocations being pulled from migrating interfaces in Ag-Al alloys.

Transformations between the β(BCC) and ξ(HCP) phases revealed that dislocations were emitted into the β phase. The dislocation generation was associated with the relaxation of transformation strains and the presence of step-type interfacial defects. The dislocations were also observed to be absorbed in the same boundary which generated them on further transformation. The induced dislocation generation contributed to the development of a non-uniform boundary migration and a modified boundary morphology at high undercoolings. The net effect of the dislocation/boundary interaction is to influence the interfacial reaction kinetics during a phase transformation.

1.2.2(b) Carbide Morphology and Precipitation

The basic effect of alloying elements is to influence the carbide morphology by altering the γ/α reaction and by changing the composition and structure of the carbide phase(35).

Molybdenum is by no means an exception to the rule. In fact it can and does appear in a number of structures and morphologies. The most common(42) are the stoichiometric forms MoC and Mo_2C, both hexagonal where the former has alternate layers of metal and carbon atoms and the latter has the metal atoms in the CPH positions and the carbon atoms in alternate layers in the octahedral interstices. The other forms of carbides are $(Fe, Mo)_6C$ and the $(Fe,Mo)_{23}C_5$ which are both complex cubic with very large unit cells, the former containing 95 metallic atoms and the latter containing 92.

Several investigators(36-40) have documented the occurrence of these carbides both in structure and morphology. The most common form is that of Mo_2C, and it has been found to occur in the form of fibres, needles, and rows of interphase carbide precipitates. The formation of these precipitates by interphase precipitation has been dealt with in a review paper by Honeycombe(35). The row precipitates have been found in conjunction with faceted γ - α interfaces. They nucleate on the steps and are subsequently overgrown by the risers. The fibrous carbides are associated with non-faceted interfaces. Barbacki and Honeycombe(43) suggest that it is the transformation temperature which will dictate the predominate carbide morphology. At lower reaction temperatures the $\gamma - \alpha$ interfaces changed from faceted to smooth with a corresponding change in the morphology of carbide precipitation. The most recent work by Purdy(40) indicated that at higher transformation temperatures, fibrous carbides were found to form at the $\gamma - \alpha$ interfaces. He did find that they tended to form after a great deal of ferrite had precipitated, i.e., late in the transformation, and the carbides were widely spaced. The formation was also noted to be sporadic which resulted in carbide-free bands.

On lowering the transformation temperatures, the spacing of the fibres and raw carbides was decreased.

Honeycombe(35) in his review paper makes some general statements regarding carbide precipitate nucleation and growth:

1) Bands are parallel to γ/α boundaries and the bands will follow changes in the boundary.
2) Direct observations have shown that carbide particles nucleate on the interface.
3) Carbide particles are frequently only in one variant of a Widmanstätten habit.
4) Orientation relationship of the carbides with the ferrite matrix are the same as those encountered in tempered martensites. For Mo_2C particles:

$$(011)\ \alpha \parallel (0001)_{Mo_2C}$$

$$(100)\ \alpha \parallel (2\bar{1}\bar{1}0)_{Mo_2C}$$

$$[100]\ \alpha \parallel [2\bar{1}\bar{1}0)_{Mo_2C\text{(growth direction)}}$$

The mechanism of growth of the ferrite associated with the interphase precipitation is predominantly by the ledge mechanism. Aaronson(44,45) and coworkers have established this mechanisms as well for ferrite with no precipitates.

Some experiments by Honeycombe(35) on an Fe-12Cr-.02C isothermally transformed between 650-750°C produced ledges about 50 - 400 nm, large enough to be resolved in the transmission electron microscope. He observed that the nucleation did not take place on the ledge, but on the planar boundary (Fig. 1.13). This was a reversal of normal nucleation. Further analysis revealed that the boundary plane was of $\{110\}_\alpha$ nature, probably low energy with corresponding limited mobility. Hence the growth of ferrite would occur by swift migration of a number of incoherent high energy steps. In light of the high energy of the steps, these should be favorable positions for nucleation, but the mobility of ledges precludes this. Hence the nucleation was found to occur on the low energy low mobility planar faces as they extend due to ledge migrations. Micrographs showing the decreasing size of precipitates and clearly indicating the sequence of nucleation have been documented(35).

The development of spacing and banding in the precipitates is controlled by the spacing of the ledges (Fig. 1.13). Rigsbee and Aaronson(44) did some computer modelling of ledge growth, in terms of best fitting the atoms of the matrix and the growing phase, in this case austenite-ferrite. This type of modelling could be useful in sorting out the banding that can occur as a result of ledge growth.

The morphology of carbides has been found to vary within a steel and even with a single austenite grain. The fine fibrous carbide normally form from high energy boundaries in the austenite, the interphase

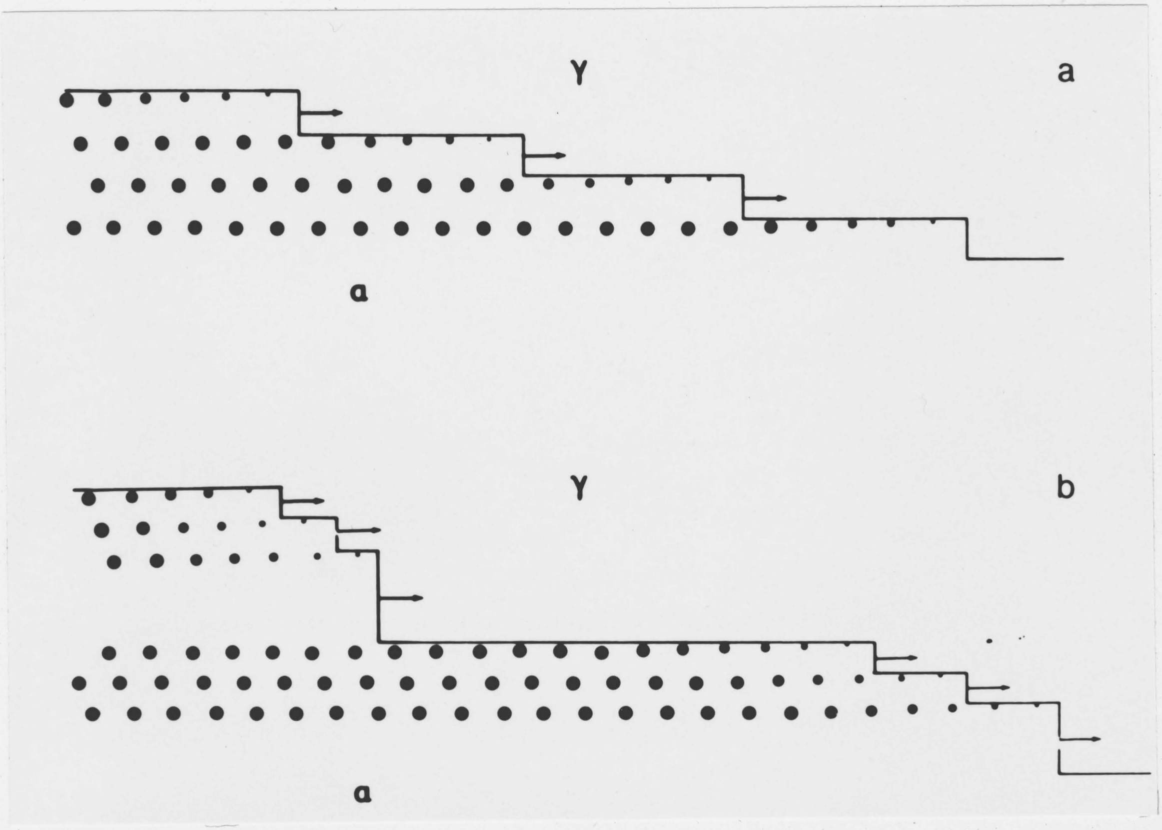

Fig. 1.13 Mechanism for the nucleation and growth of carbides on the γ/α interface. (Honeycombe[35])

reaction is associated with the movement of high energy steps on low energy planar boundaries. It is also expected in light of the energetics that in the latter case the growing ferrite in the austenite would be related by the K - S relation.

CHAPTER 2

EXPERIMENTAL PROCEDURES

To study the effect of molybdenum on the proeutectoid ferrite reaction some simple isothermal and continuous cooling heat treatments were carried out on four iron-carbon-molybdenum alloys - see Table 2.1 The structures which were produced were then studied using optical and electron metallography. Some transformations were also carried out on some tensile test specimens so the mechanical strength could be evaluated.

2.1 Material

The alloys used were iron carbon molybdenum alloy, chemical composition as described in Table 2.1. The alloys were produced by Climax Molybdenum in their vacuum melting facility. The heats were carbon deoxidized under vacuum using .03% Al to assist the deoxidation. The ingots were then hot rolled to plates - approximately 250 mm x 300 mm x 13 mm.

A binary iron carbon alloy was also used as a comparison to the Fe-C-Mo in one part of the experimental program. This alloy was a high purity Fe-C alloy produced at the Falconbridge research laboratories and hot forged at the Department of Energy, Mines and Resources in Ottawa.

2.2 Continuous Cooling

The first transformation studies carried out were on the products

Table 2.1 Chemical Composition.

Alloy No.	Heat No.	Composition (wt.%)		
		C	Mo	Al
1	1827	0.05	0.99	0.02
2	1837	0.18	0.98	0.02
3	1838	0.28	1.00	0.02
4	1839	0.43	1.00	0.02
5		0.355	0.00	0.00

Notes: 1) Alloys 1 - 4 courtesy of Climax Molybdenum.

2) Aluminum used to deoxidize the steel.

of continuous cooling. This was done to determine the range of cooling rates under which proeutectoid ferrite product forms as grain boundary allotriomorphs and idiomorphs(1).

To enable the use of predetermined cooling rates in continuous cooling experiments, Jominy test specimens were used. However, the diameter of the material was inadequate to make the standard stamples, so X Jominy bars of plain carbon steel (commensurate with the carbon content of the molybdenum alloys) were drilled out and a rod of molybdenum alloy was inserted into each bar. The molybdenum rods were initially swaged to .25" diameter from .5" and were then sealed off under vacuum (10^{-5} torr) in quartz and homogenized for 96 hours at 1200°C; the alloys were subsequently quenched in water. The alloy rod was then inserted into the Jominy test specimen (Fig. 2.1(a)) and a standard ASTM Jominy End Quench test was carried out. The Jominy test specimens were cut in half (lengthwise) and the alloy rods removed. The rods were then prepared for and observed with light microscopy.

This was done for each of the four alloys being studied.

2.3 Isothermal Transformation

The isothermal transformation treatments were conducted using conventional salt baths at the required temperatures.

The sample shape and size used in these experiments was approximately .5 cm by 1 cm diameter discs. This shape was chosen to provide a large surface area to aid the heat transfer on quenching to salt bath temperatures.

Prior to heat treatment the 1 cm rods of alloy were sealed off in quartz capsules and homogenized for 96 hours at 1200°C after which they were quenched in water.

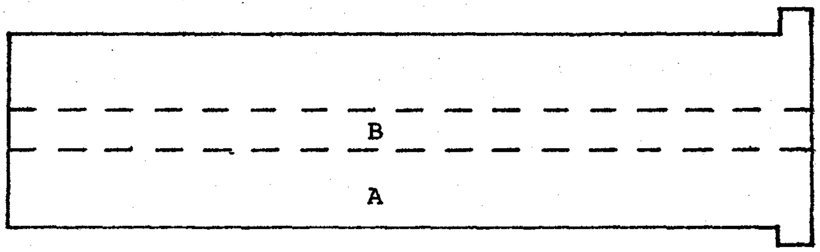

A - Plain Carbon Steel
B - Fe-C-Mo Alloy

Figure 2.1(a) ASTM Jominy specimen with alloy insert

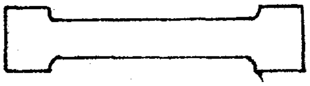

Figure 2.1(b) Tensile Specimen

Note: Drawn to scale

The isothermal transformations were carried out at 650°C for times as specified in Table 2.2 for the particular alloy. This followed an initial austenitizing and grain growth treatment at 1200°C for 30 minutes. Large austenite grains were formed in order that the ferrite crystals which nucleated and grew could be simply observed. It was found with smaller grain sizes that impingement of the growing crystals prohibited a thorough investigation of the growth process.

After the isothermal treatment the samples were mounted and polished for examination with the optical microscope. Some of these samples were also observed on the transmission electron microscope.

2.4 Microstructural Stability

Some experiments were designed to test the stability of the substructure of the proeutectoid product formed at 650°C.

Two materials, a binary Fe-C (5) alloy and a ternary Fe-C-Mo (4) alloy were used to study and compare the effect of Mo on the stability of the microstructure and substructure. An attempt to determine the equilibrium shape of proeutectoid ferrite crystals in both binary and ternary alloys was made.

The samples of material (4,5) were sealed off in quartz capsules under vacuum to prevent decarburization and oxidation at high temperatures. The procedure following was the same as for the isothermal treatment except instead of being quenched the samples were taken up to a temperature in the two-phase region ($\gamma + \alpha$) to form microstructures consisting of approximately 20% ferrite and 80% austenite. The samples were left at these temperatures (772°C - Fe-C-Mo and 780°C - Fe-C) for fourteen days for which time diffusion calculations indicated a diffusion distance of 2 mm (which was greater than the grain diameter). Duplicate samples

Table 2.2 Isothermal heat treatment schedule.

Alloy	Time at 650°C
1 (a)	10 sec.
(b)	20 sec.
(c)	2 min.
(d)	4 min.
2 (a)	30 sec.
(b)	60 sec.
(c)	2 min.
(d)	5 min.
3 (a)	5 min.
(b)	10 min.
(c)	20 min.
(d)	40 min.
4 (a)	5 min.
(b)	10 min.
(c)	20 min.
(d)	30 min.
(e)	60 min.

were quenched in water to ensure that the microstructure after the initial isothermal treatment was the same as the samples which were not sealed off in quartz capsules but underwent the same thermal treatment and the microstructures were compared.

Both alloys were, after the equilibration treatment, prepared for and observed using optical metallography.

The metallography was done with both reflected light and transmission electron microscopes. Standard polishing techniques and etching, using nital and picral etchants, were used for the optical metallography.

The specimens for the transmission electron microscope (Philips EM300) were prepared two ways:

1) Surface replicas - both one-stage carbon and two-stage collodium replicas produced by standard techniques.
2) Thin foils - thin slices were cut, ground and polished to a thickness of .004", then chemically polished in a solution of approximately 85 ml H_2O, 5 ml H_2O_2 and 10 ml HF. Final polishing was done electrolytically using a Streurs "Tenupol" with a 90% methanol, 10% perchloric acid electrolyte.

2.5 Mechanical Testing

Mechanical testing involved microhardness and tensile testing of the four Fe-C-Mo alloys.

The microhardness was done using a Tukon Microhardness Tester fitted with a Vickers diamond pyramid indenter. The load chosen increased with carbon content of the alloys, to stay in the reliable operating limits of the machine.

These measurements were used two ways: to find the hardness of the wrinkled ferrite relative to the clean ferrite which forms on isothermal transformation; and, to aid in differentiating the structures in the continuously cooled specimens.

Some of the mechanical properties of the Fe-C-Mo alloys were also studied using data obtained from tensile tests. The configuration of the tensile specimens used is shown in Fig. 2.1(b).

The alloys were isothermally heat treated in salt baths but were austenitized at a lower temperature (1000°C) for a shorter time (15 min.) to obtain a smaller grain size.

The tests were done using a 10,000 lb Instron machine, with the load set at 5,000 lb and an extension rate of .01"/minute.

CHAPTER 3

EXPERIMENTAL RESULTS

3.1 Continuous Cooling

A survey of the four Fe-C-Mo alloys in terms of microstructure and microhardness was completed and the results are summarized in Figs. 3.1(a) - 3.4(d).

In continuous cooling experiments one expects to obtain a spectrum of microstructures, starting with martensite at the quenched end and progressing through bainite and Widmanstätten ferrite with increasing distance from the quenched end (increasing distance implies decreasing or slower cooling rates).

The structures which formed in the four Fe-C-Mo alloys were within this spectrum of microstructures. In Figs. 3.1 - 3.4(a) the structure of the quenched end is illustrated for the alloys with hardness measurements below. The structure is martensitic and the hardness shows that the effect of lowering the carbon content is to decrease the hardness.

The following series of figures (Figs. 3.1 - 3.4(b)) illustrate two points: overall the structure the laths appear to coarsen and ferrite allotriomorphs and idiomorphs(1) as indicated by the arrows, begin to appear. The hardness numbers indicate a larger drop for the high carbon specimens as compared to low carbon specimens.

The next series of structures illustrates an important effect of

Figs. 3.1 - 3.4

Continuous cooling transformation structures.

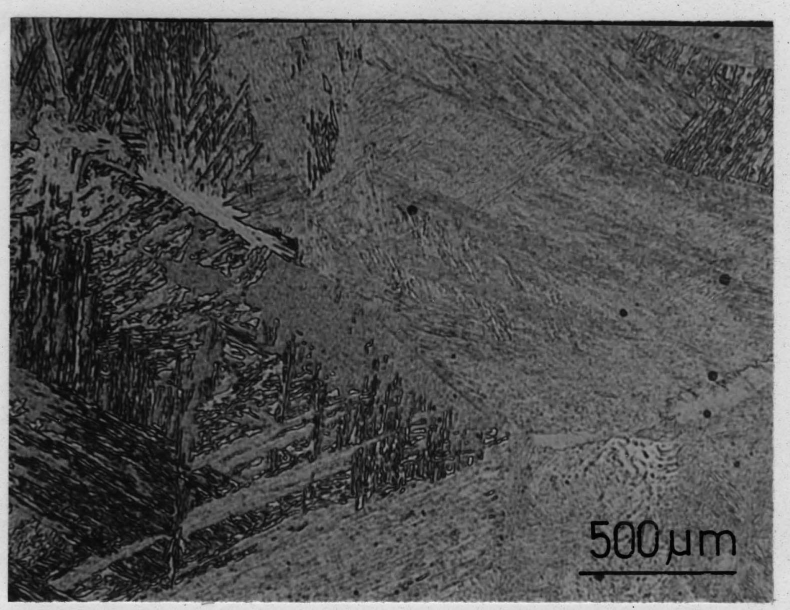

Fig. 3.1(c) Alloy 1 - 1/4" from quenched end.
Hardness 216 DPH.

Fig. 3.1(d) Alloy 1 - 5/8" from quenched end.
Hardness 200 DPH.

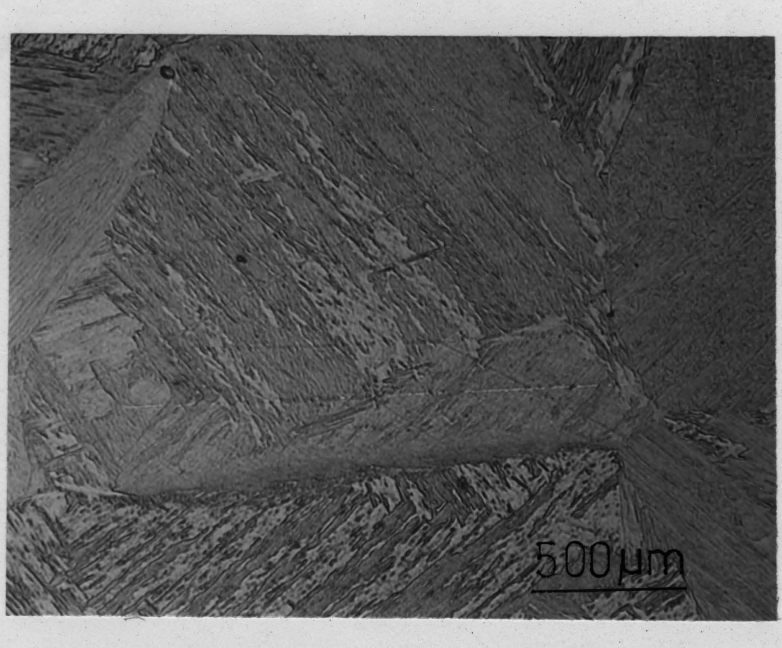

Fig. 3.2(a) Alloy 2 - 1/16" from quenched end.
Hardness 339 DPH.

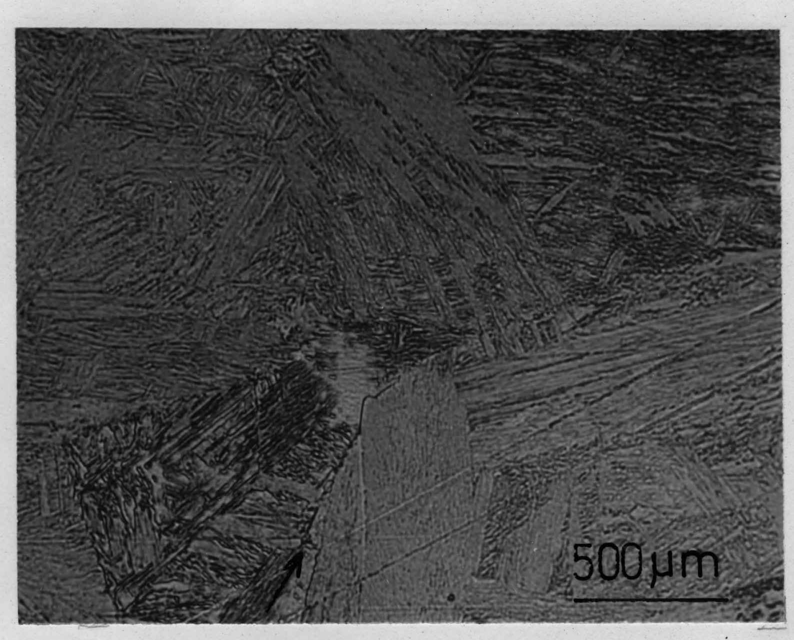

Fig. 3.2(b) Alloy 2 - 1/8" from quenched end.
Hardness 272 DPH.

Fig. 3.2(c) Alloy 2 - 1/4" from quenched end.
Hardness 236 DPH.

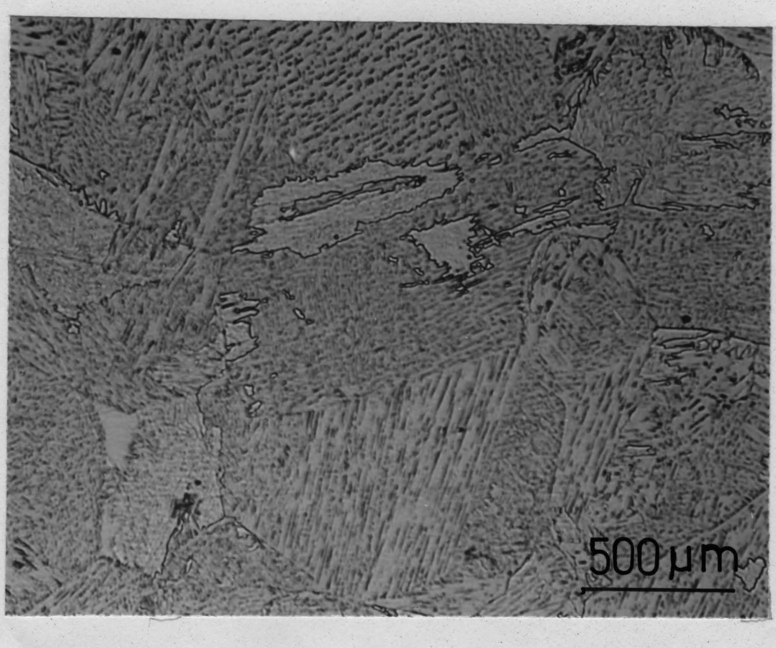

Fig. 3.2(d) Alloy 2 - 5/8" from quenched end.
Hardness 200 DPH.

Fig. 3.3(a) Alloy 3 - 1/8" from quenched end.
Hardness 426 DPH.

Fig. 3.3(b) Alloy 3 - 1/4" from quenched end.
Hardness 386 DPH.

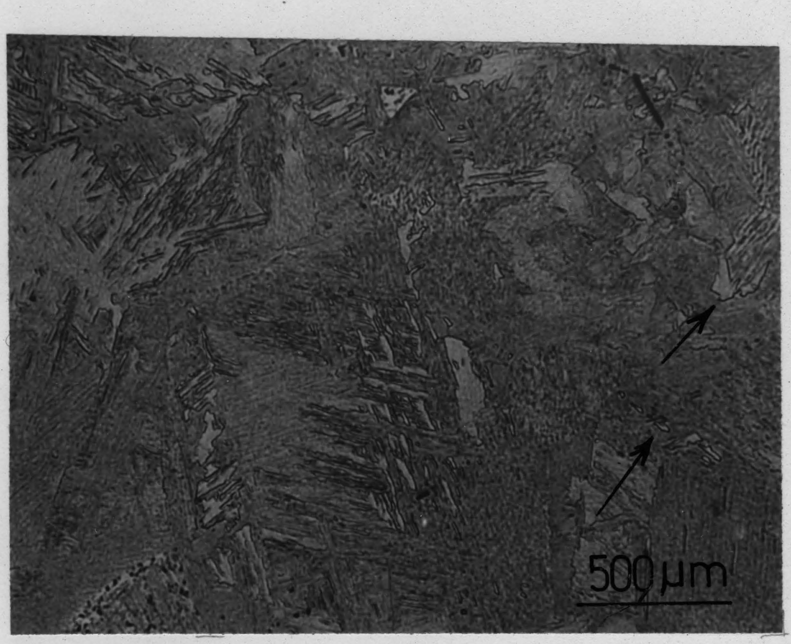

Fig. 3.3(c) Alloy 3 - 1/2" from quenched end.
Hardness 288 DPH.

Fig. 3.3(d) Alloy 3 - 5/8" from quenched end.
Hardness 264 DPH.

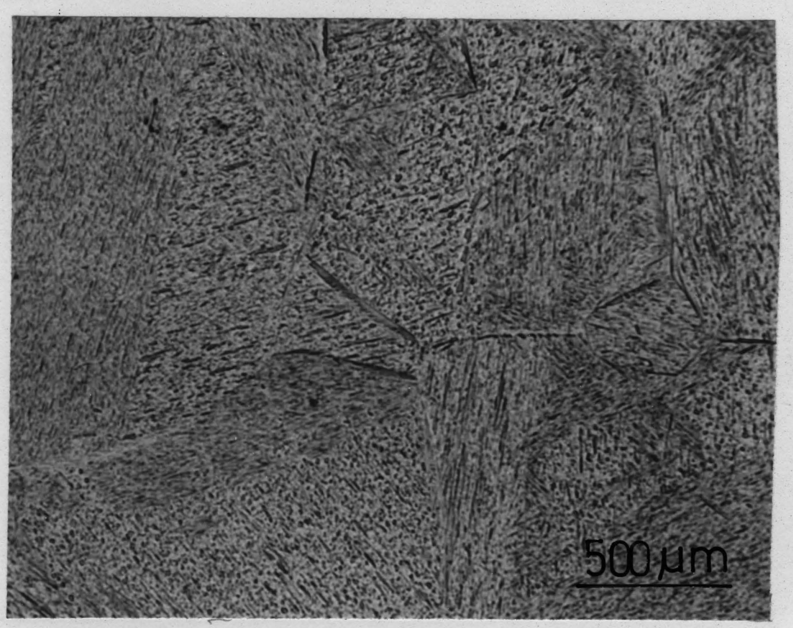

Fig. 3.4(a) Alloy 4 - 1/16" from quenched end.
Hardness 653 DPH.

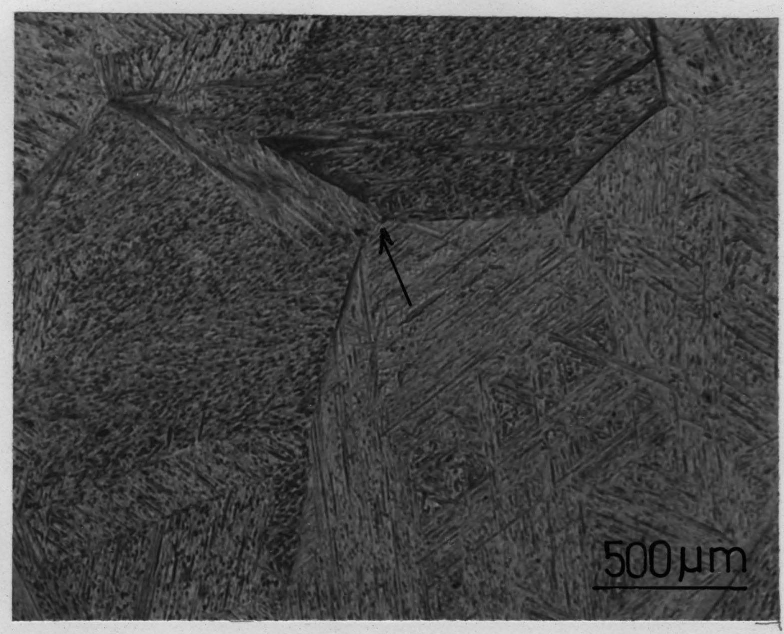

Fig. 3.4(b) Alloy 4 - 3/16" from quenched end.
Hardness 612 DPH.

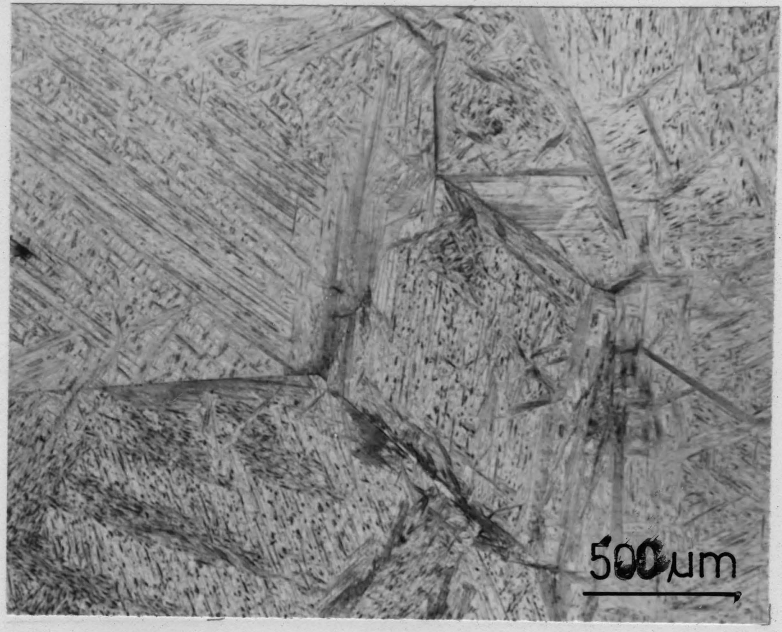

Fig. 3.4(c) Alloy 4 - 3/8" from quenched end.
Hardness 505 DPH.

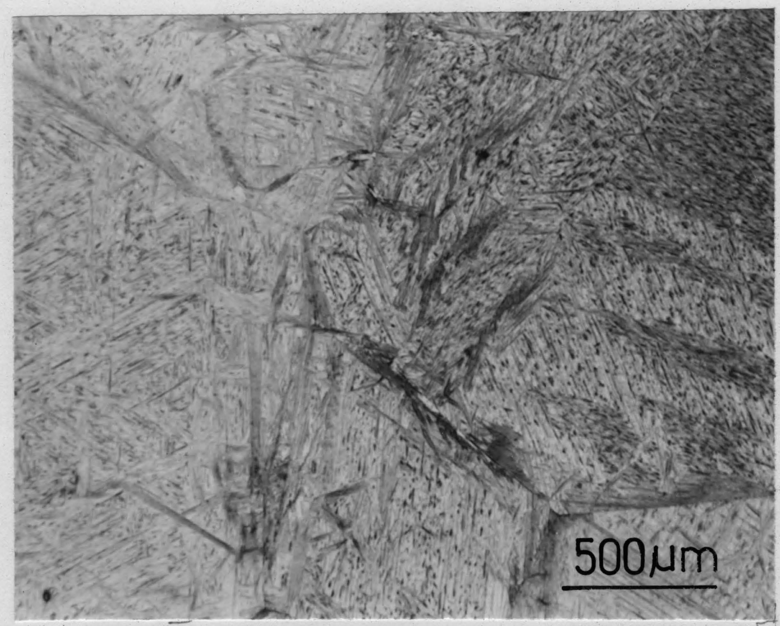

Fig. 3.4(d) Alloy 4 - 5/8" from quenched end.
Hardness 389 DPH.

carbon content. In the two lowest carbon alloys, Figs.3.1(c) and 3.2(c) the structure is a mixture of grain boundary ferrite, ferrite idiomorphs and a Widmanstätten structure. By observing the structures of Figs. 3.1 (d) and 3.2(d) it is evident that the type of structure is similar, but the proportions of each are changed; this shows that there is no sharp transition between these structures. The hardness also indicates this by the lack of a significant decrease.

The two higher carbon alloys as illustrated in Figs. 3.3(c) and 3.4(c), show a more decisive separation of structures. In Fig. 3.3(c) the left side of the micrograph is predominantly coarse Widmanstätten ferrite while the right side is much finer with some grain boundary allotriomorphs (indicated by arrows). Fig. 3.3(d) is a typical microstructure of the rest of the test specimen, very coarse Widmanstätten ferrite. In Figs. 3.4(c) and 3.4(d) the distance at which the structure coarsens is well defined as illustrated by the very coarse laths in the centre of both of these micrographs.

The microhardness measurements for these two alloys are commensurate with the micrographs, that is, significant decreases in hardness are evident where the structures change; that is, a decrease in hardness number with coarser structures.

3.2 Isothermal Transformation

The effect of isothermally transforming the Fe-C-Mo alloys at 650°C is to produce a dark etching proeutectoid ferrite phase. In Fig. 3.5 the microstructure of an Fe - .43% C - 1% Mo alloy is illustrated after being transformed at 650°C for 40 minutes. The microstructure is a mixture of the dark etching constituent known as "wrinkled ferrite", clean ferrite and martensite (labelled A, B and C respectively).

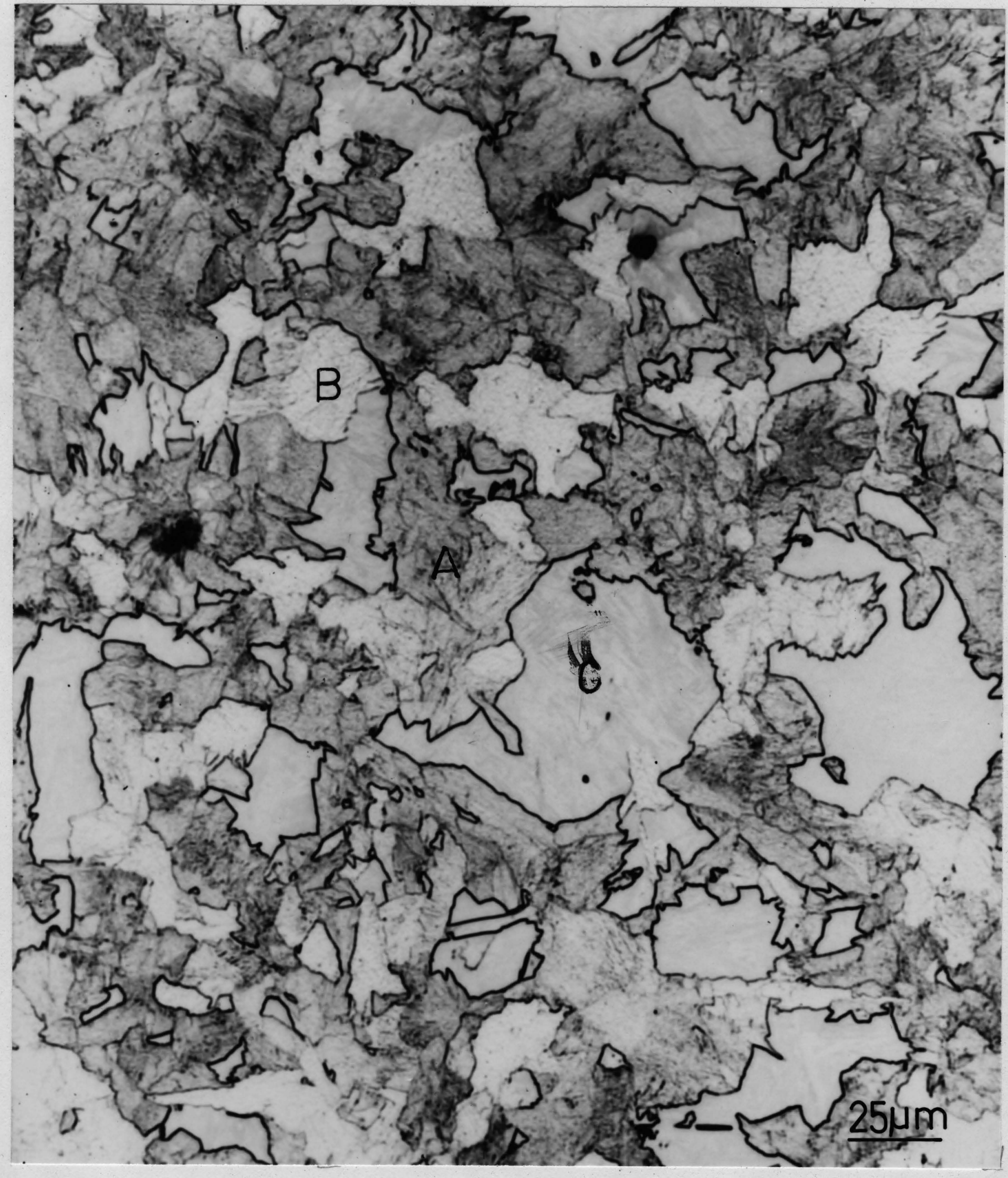

Fig. 3.5 Alloy 4 - Austenitized at 1050°C for 30 minutes, quenched to 650° and held for 40 minutes followed by a water quench. A, B and C indicate wrinkled ferrite, clean ferrite and martensite, respectively.

Transmission electron microscopy studies of the transformed microstructure indicated that the structure of the wrinkled ferrite is due to a high density of dislocations, as illustrated in Fig. 3.6 (after Purdy(40)). A large number of carbides in several morphologies and in different regions are also found. The predominant carbide is Mo_2C which occurs as fibres (Fig. 3.7, after Purdy(40)), needles (Fig. 3.8) and fine precipitates (Fig. 3.9). The fibrous and needle morphologies are generally found in the ferrite close to the α/γ transformation interface. The fine precipitates are found as intraphase and interface precipitates, illustrated in Figs. 3.9 and 3.10 respectively.

Using the four Fe-C-Mo alloys, a series of isothermal transformations at 650°C were conducted for increasing times; the schedule was as given in Table 2.2.

The following micrographs, Figs. 3.11(a) through 3.14(e) are representative of the microstructures of the alloys corresponding to the isothermal reaction time given in Table 2.2. The structures obtained after the shortest reaction time for the four alloys are shown in Figs. 3.11 - 3.14(a). In all four of the alloys the ferrite is found on the prior austenite grain boundaries, the matrix being martensite as a result of quenching. The ferrite appears to nucleate and grow initially as small blocks on the interface which spread to completely cover the austenite grain boundaries. The morphology of the initial ferrite crystals is a smooth planar interface on one side of the boundary and a jagged irregular interface on the other side.

The average grain diameter in this series of micrographs (Figs. 3.11(a) - 3.14(e) is the order of 1 mm. This large grain size permits the observation of growth of the ferrite crystals without transgranular

Fig. 3.6 TEM micrograph of "wrinkled ferrite" illustrating the high dislocation density. After Purdy(40).

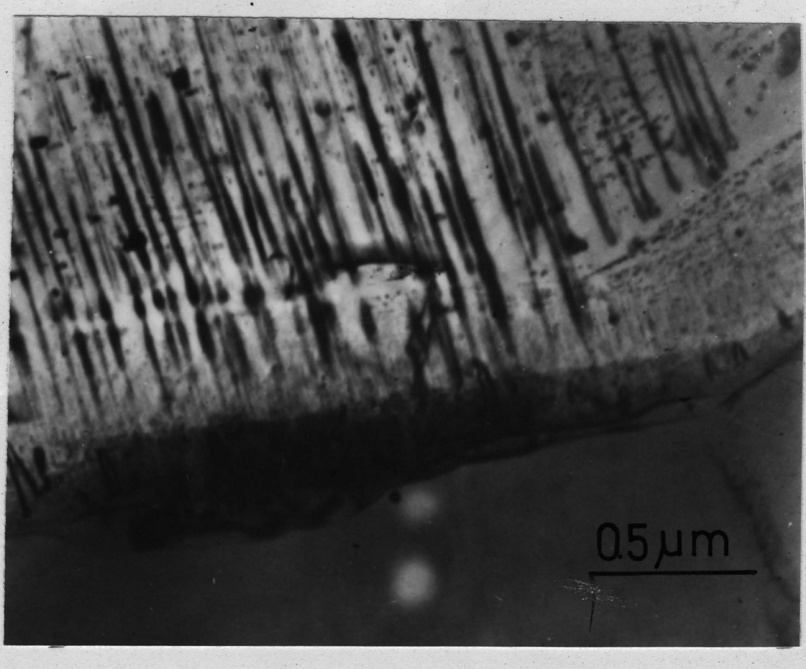

Fig. 3.7 TEM micrograph showing fibrous carbide morphology. After Purdy(40).

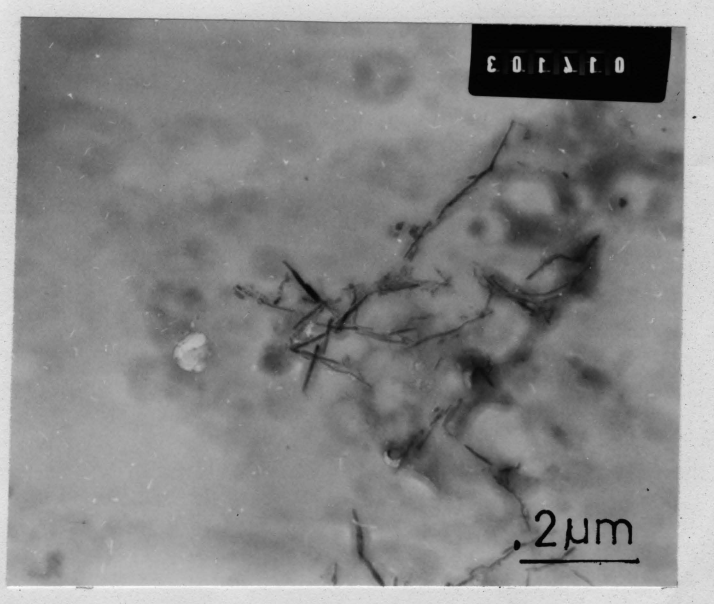

Fig. 3.8 Extraction replica showing needle carbide morphology (TEM micrograph).

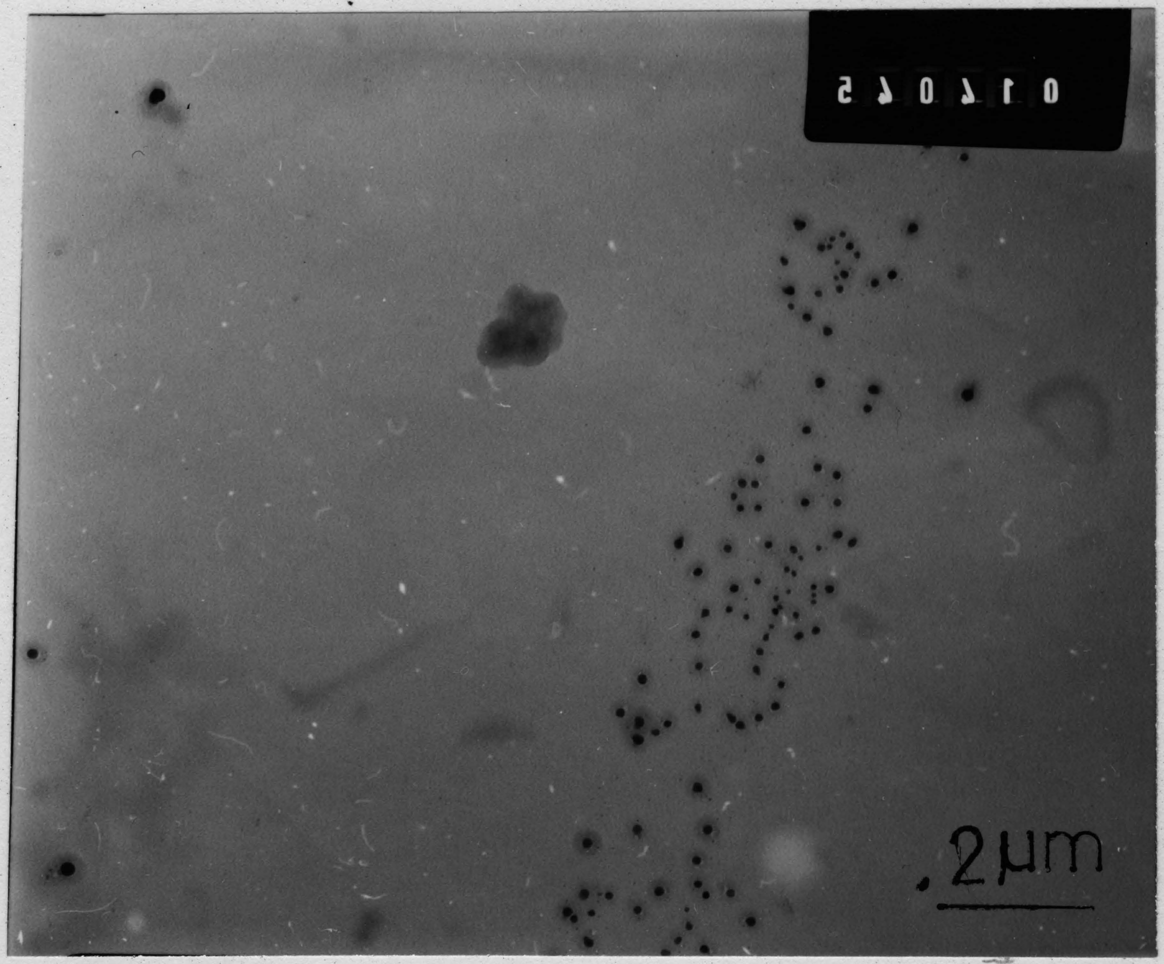

Fig. 3.9 TEM micrograph showing fine carbide precipitates.

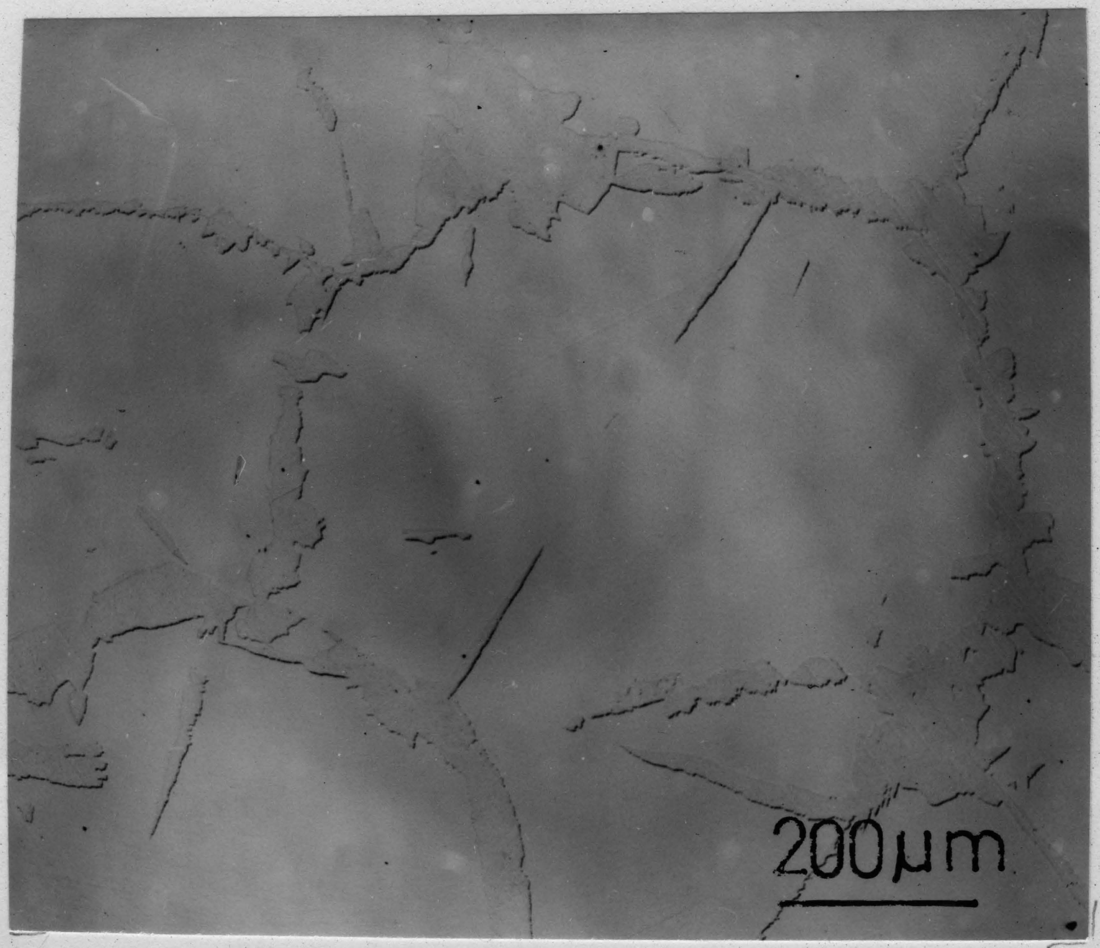

Fig. 3.10 Optical micrograph showing interfacial carbide precipitates.

Figs. 3.11 - 3.14

Isothermal transformation structures.

Fig. 3.11(a) Alloy 1 - 10 seconds at 650°C.

Fig. 3.11(b) Alloy 1 - 20 seconds at 650°C.

Fig. 3.11(c) Alloy 1 - 2 minutes at 650°C.

Fig. 3.11(d) Alloy 1 - 4 minutes at 650°C.

Fig. 3.12(a) Alloy 2 - 30 seconds at 650°C.

Fig. 3.12(b) Alloy 2 - 60 seconds at 650°C.

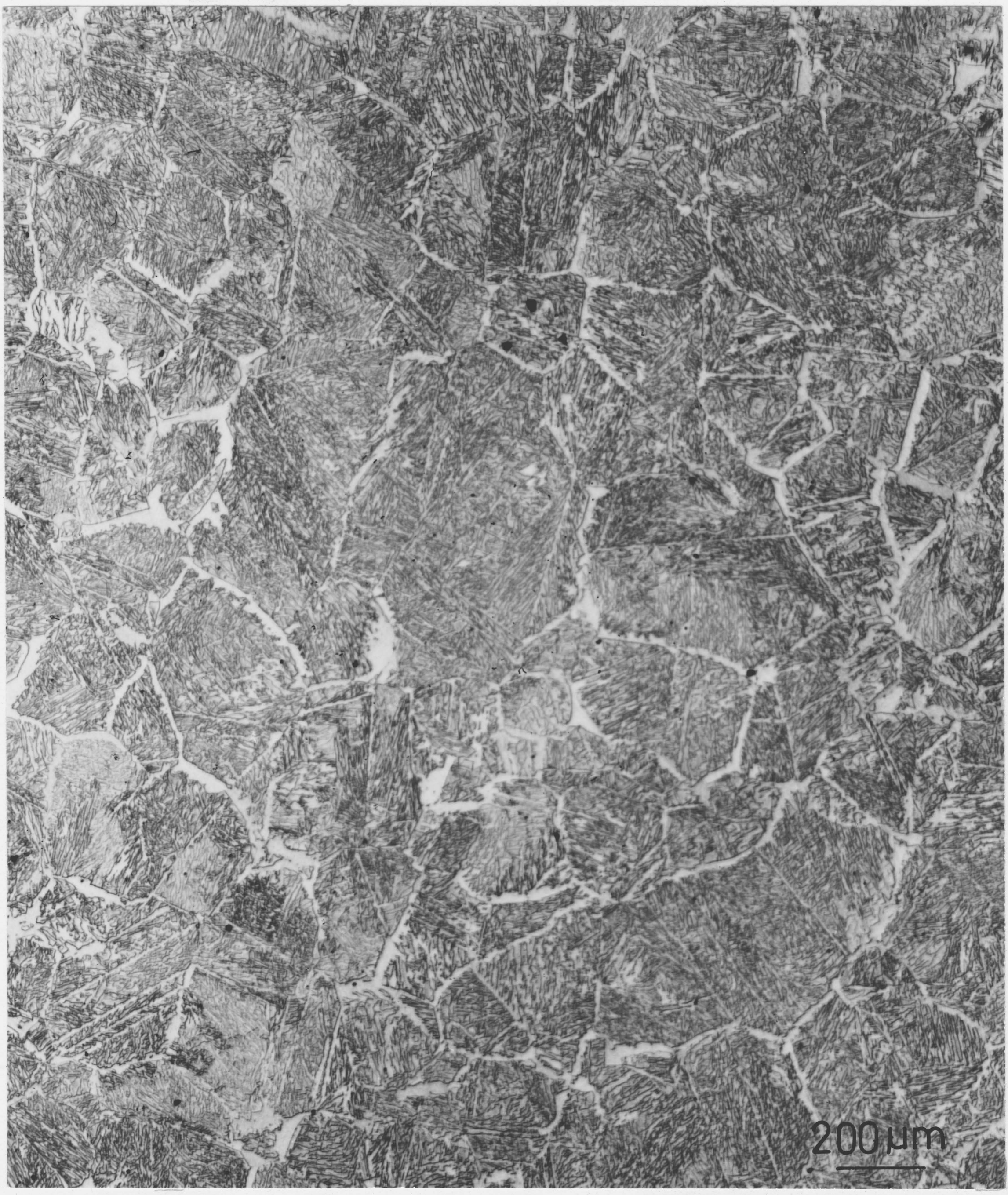

Fig. 3.12(c) Alloy 2 - 2 minutes at 650°C.

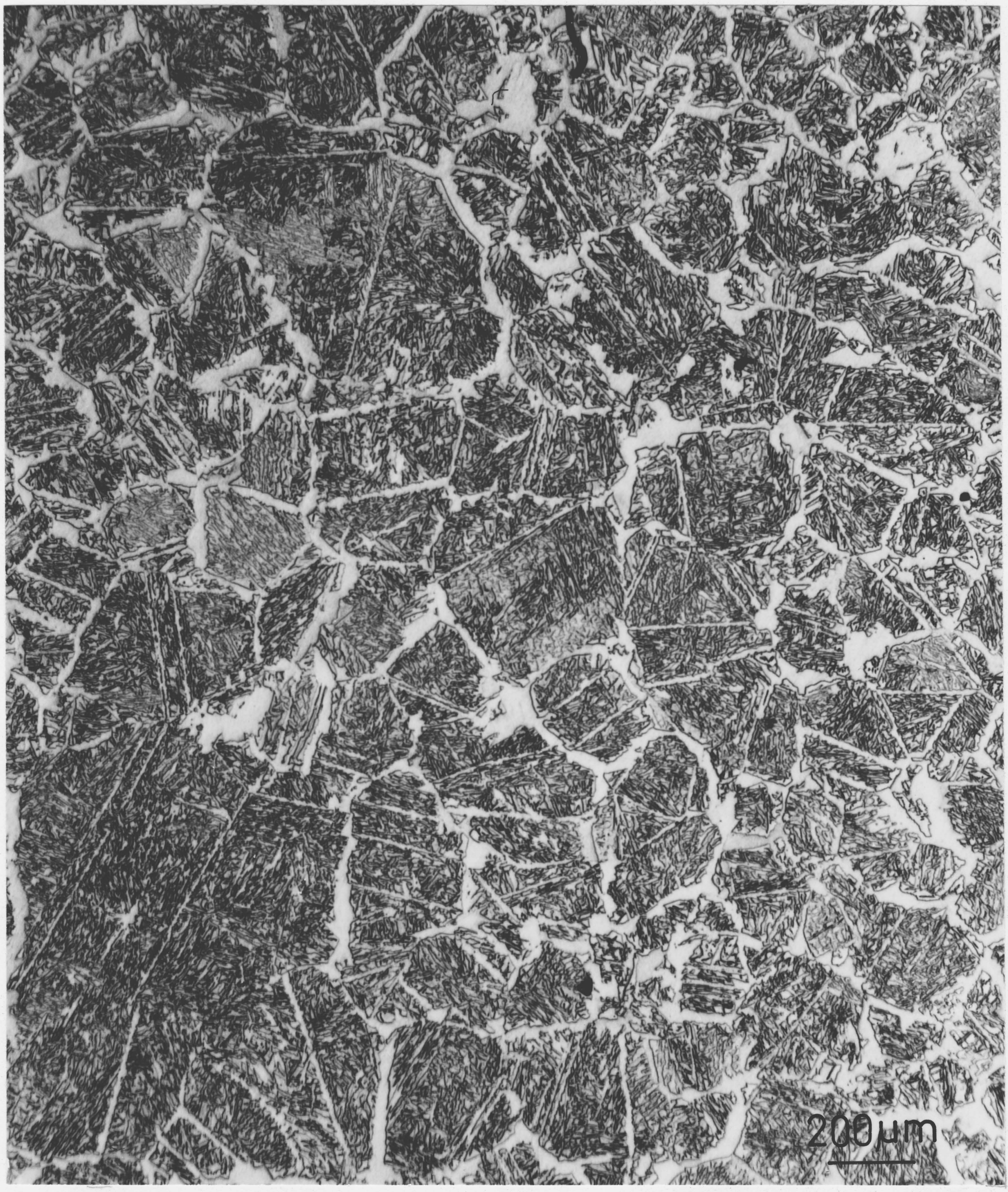

Fig. 3.12(d) Alloy 2 - 5 minutes at 650°C.

Fig. 3.13(a) Alloy 3 - 5 minutes at 650°C.

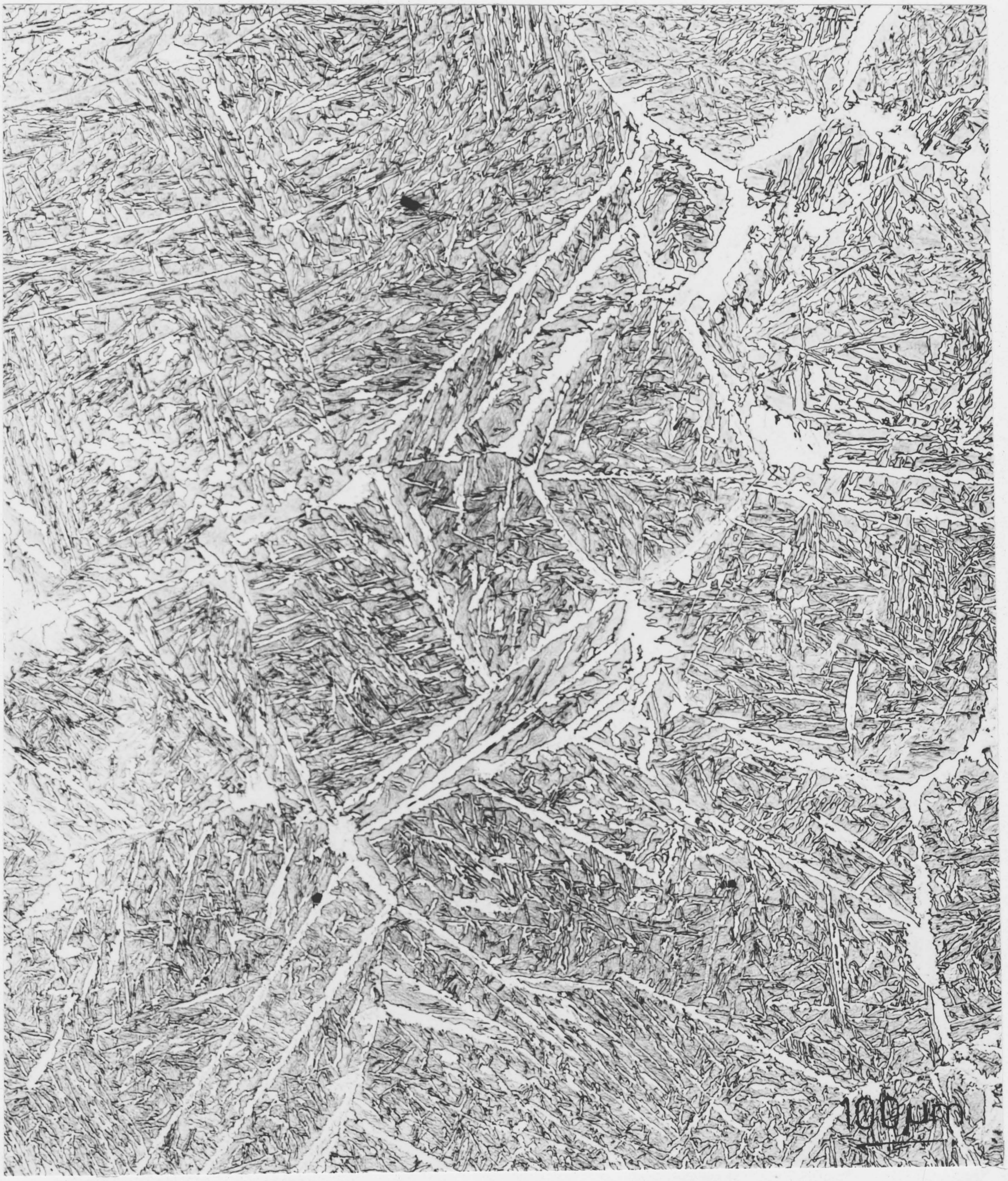

Fig. 3.13(b) Alloy 3 - 10 minutes at 650°C.

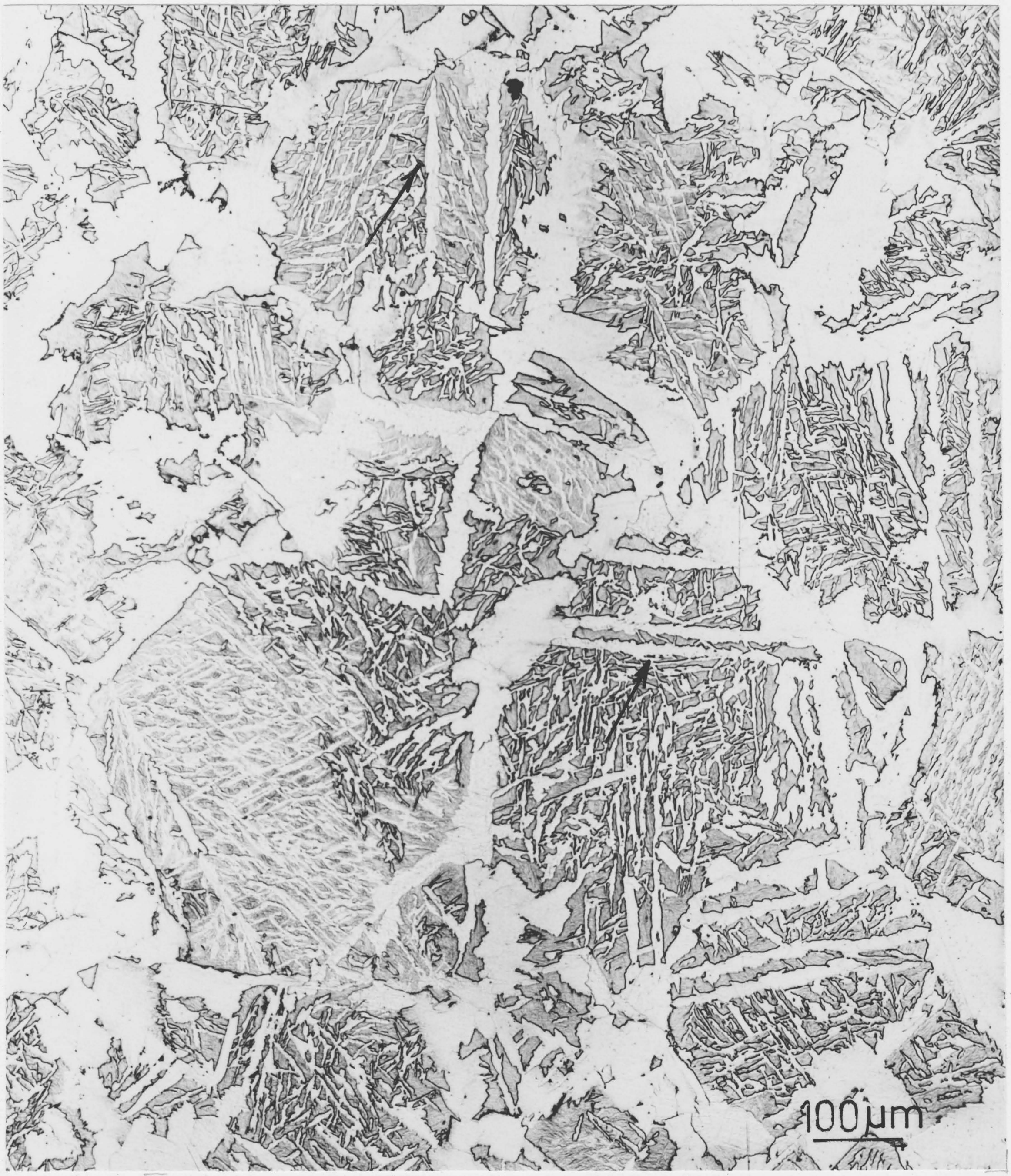

Fig. 3.13(c) Alloy 3 - 20 minutes at 650°C.

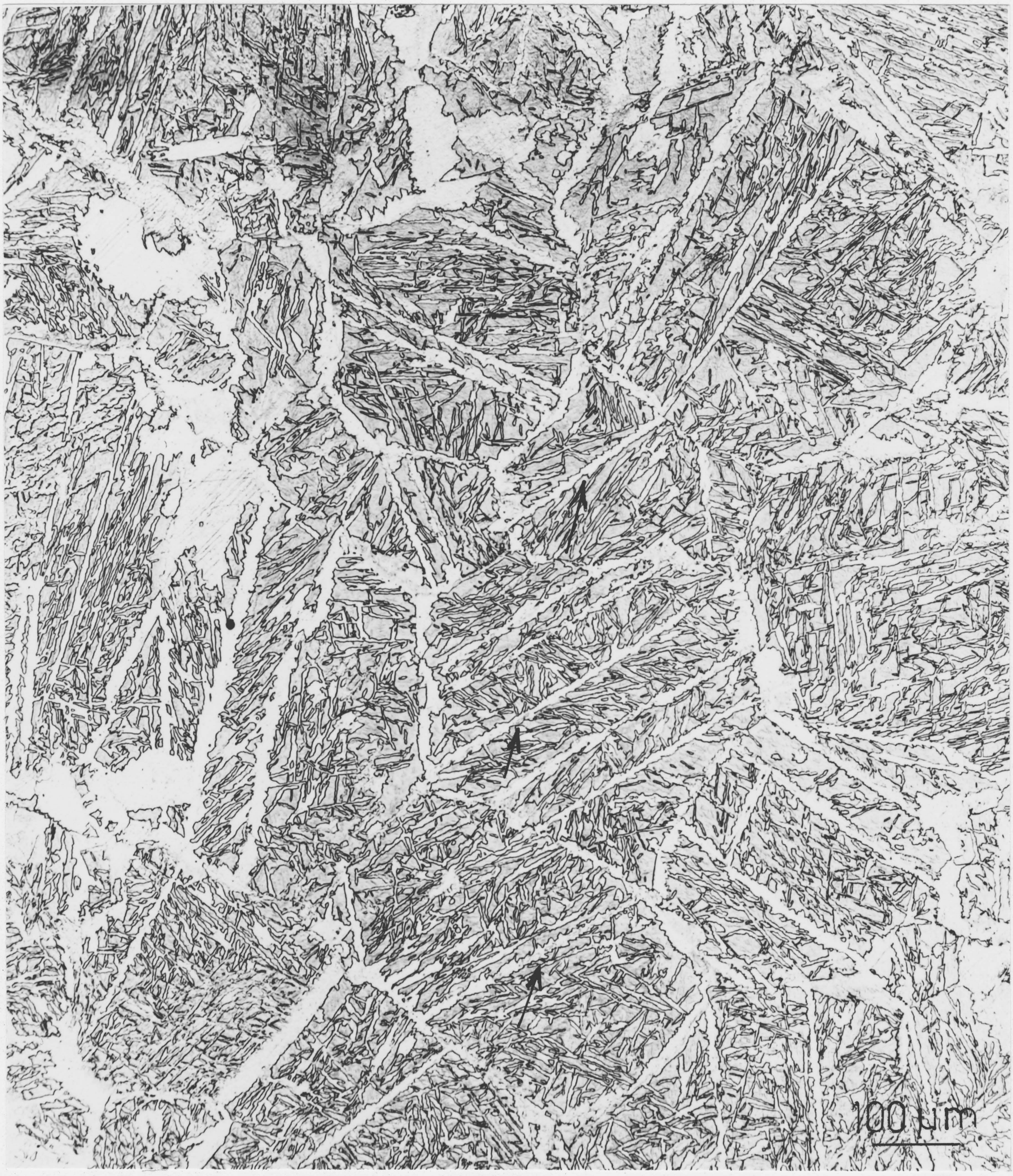

Fig. 3.13(d) Alloy 3 - 40 minutes at 650°C.

Fig. 3.14(a) Alloy 4 - 5 minutes at 650°C.

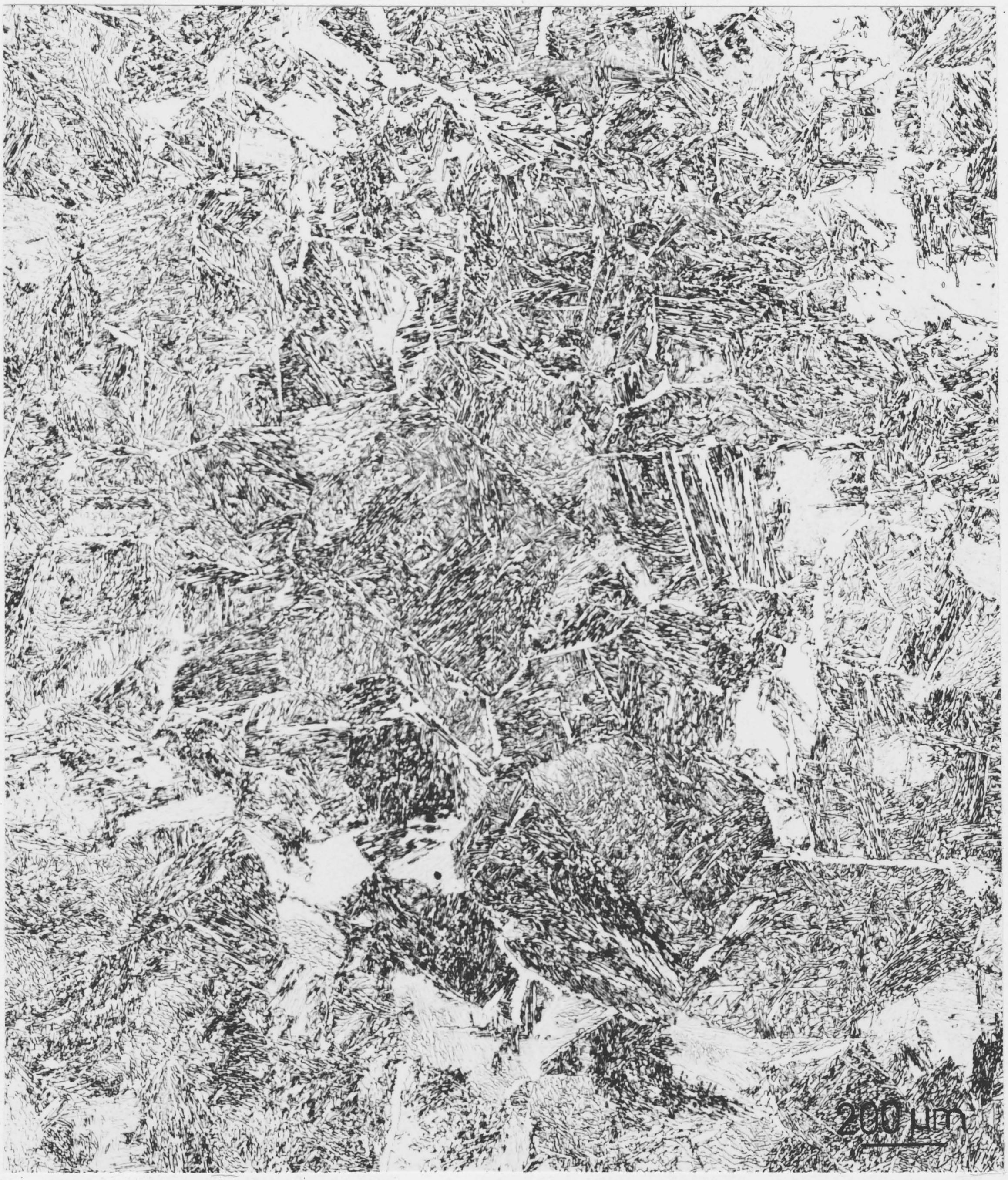

Fig. 3.14(b) Alloy 3 - 10 minutes at 650°C.

Fig. 3.14(c) Alloy 4 - 20 minutes at 650°C.

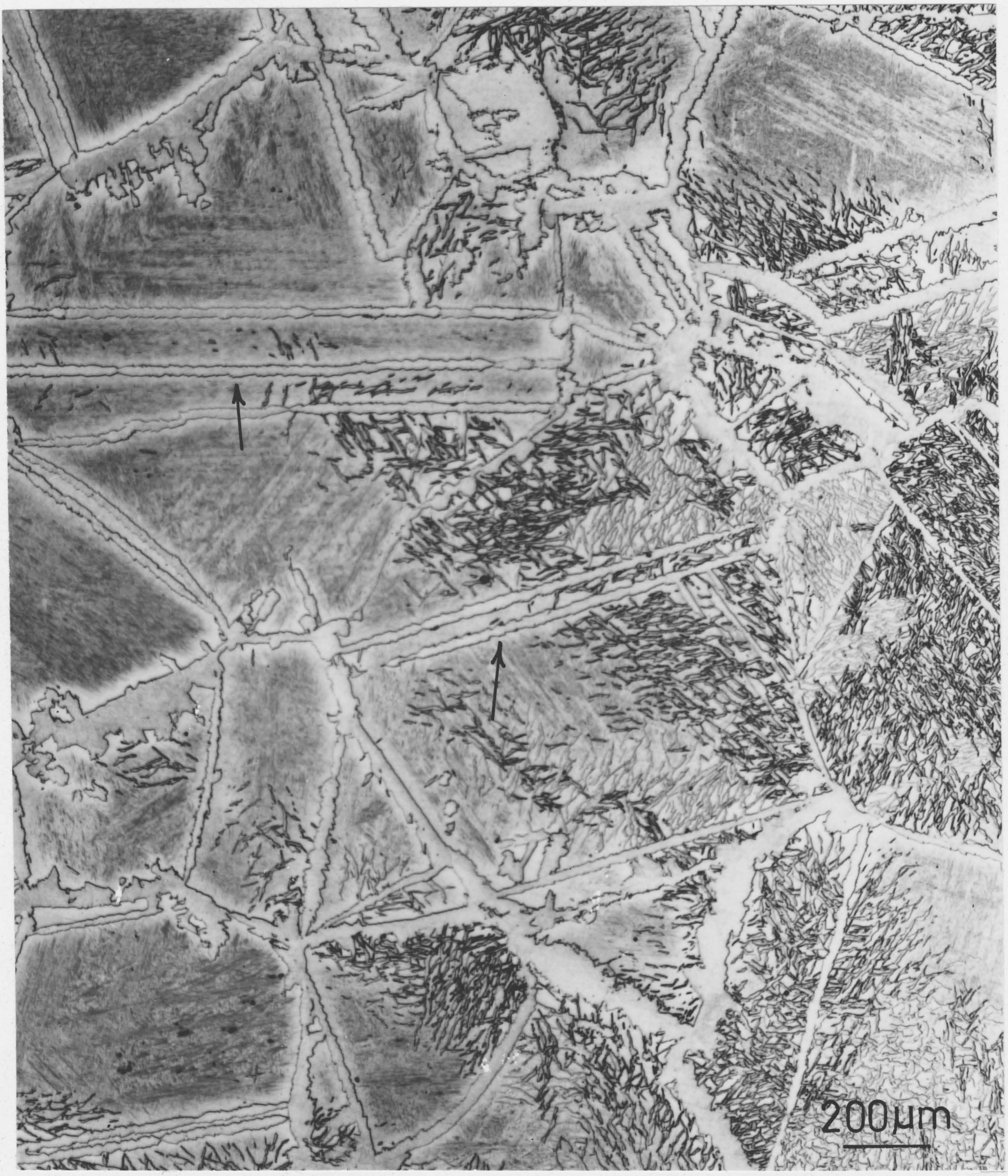

Fig. 3.14(d) Alloy 4 - 30 minutes at 650°C.

Fig. 3.14(e) Alloy 4 - 60 minutes at 650°C.

impingement of the ferrite crystals or of their diffusion fields.

On increasing the transformation time, Figs. 3.11 - 3.14(b) illustrate that the predominant effect is the impinging of ferrite crystals which had nucleated on the prior austenite grain boundaries. One very interesting feature to note in the three higher carbon alloys, Figs. 3.12 - 3.14(b) is the formation and growth of ferrite on prior twin boundaries in the austenite. The morphology of these crystals is hard to determine in the lower carbon alloy (Fig. 3.12(b) in light of the structure of the matrix, but in the higher carbon alloy the crystals appear to have planar interfaces on both sides of the twin boundary. The ferrite on the grain boundaries is continuing to grow with the morphology described earlier.

The matrix of the lowest carbon alloy (Fig. 3.11(b)) makes it impossible to discern if ferrite growth on twins occurs.

The longer tranformation times, Figs. 3.11 - 3.14 (c & d) illustrate the further growth (thickening) of the grain boundary ferrite; the original ragged interface has continued to grow in this fashion. The ferrite on the twin boundaries has also continued to thicken. Another reaction on the twin boundary ferrite is evident, the development of secondary sawteeth on the once planar interface (arrows - Figs. 3.13 and 3.14(c)). However, once the sawteeth had formed there didn't appear to be any subsequent growth of this feature, as shown by longer transformation times (arrows - Figs. 3.13 and 3.14(d)). This suggests that the sawteeth formed on quenching.

3.3 Stability and the Equilibrium Shape

The heat treatment to form the wrinkled ferrite at 650°C was followed by reheating into the $\gamma + \alpha$ range in the Fe-C-Mo system. The result of this treatment for the Fe - .43%, C - 1% Mo alloy is shown in Fig. 3.15 and

Fig. 3.15 Alloy 4 - Equilibrated at 772°C for 14 days. Note the "ghost" (carbides) at the grain boundaries and the needle-shaped ferrite.

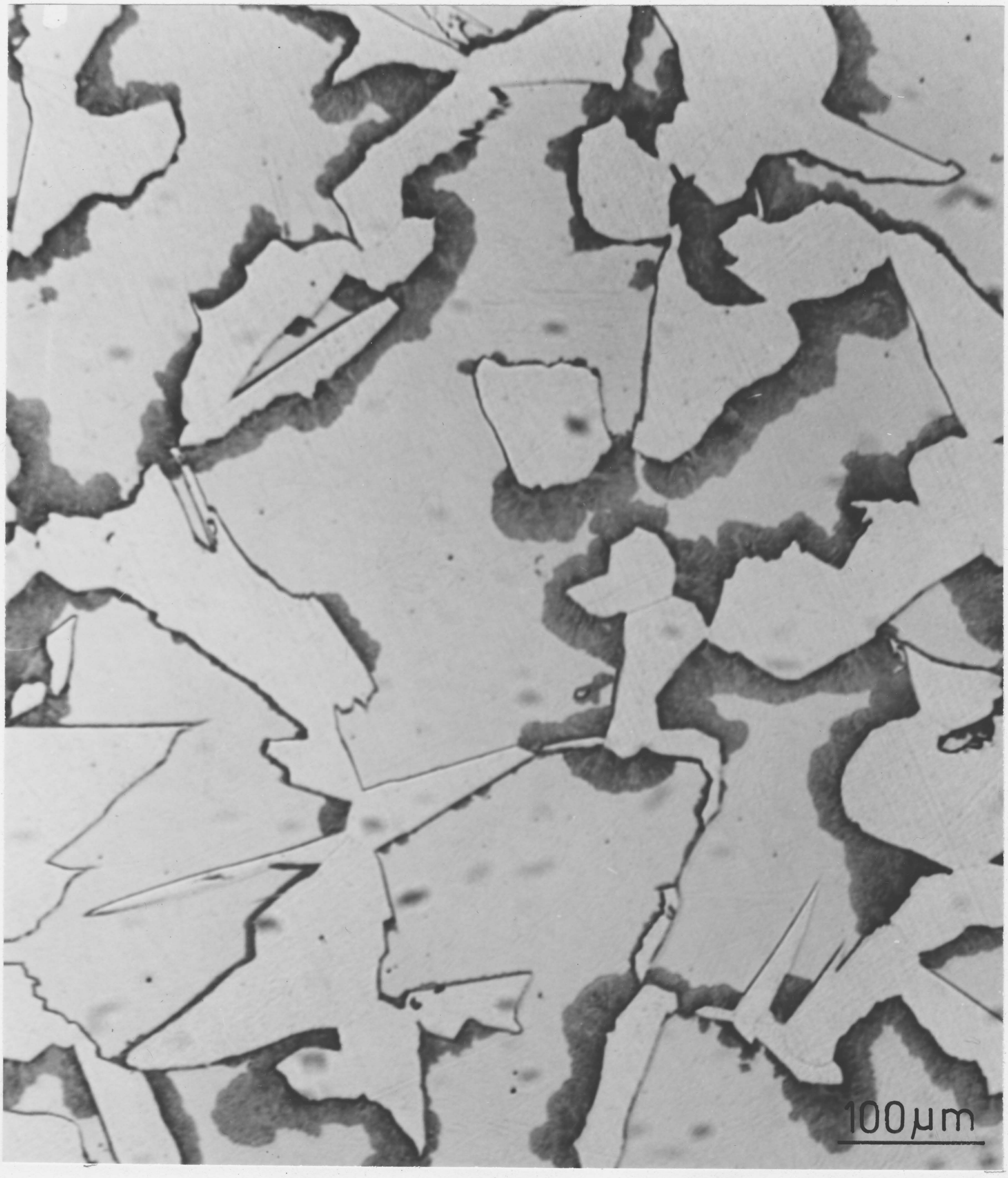

Fig. 3.16 Alloy 5 - Equilibrated at 780°C for 14 days. Note faceting of ferrite crystals.

for the Fe - .35% C in Fig. 3.16. The main differences in the microstructure for the Fe-C-Mo alloy are four. First, the ferrite which originally formed on the prior austenite grain boundaries is no longer there, but is outlined as a "ghost" on the micrograph. Second, the ferrite is in the form of intragranular crystals. Third, the ferrite is not the dark etching constituent and, fourth, the ferrite crystals have a needle-like morphology and are noticeably faceted. The binary Fe-C alloy underwent the same thermal cycle and some of the microstructural features in the transformed specimen were similar to those found in the Fe-C-Mo alloy. These include the formation of intragranular ferrite idiomorphs and faceting of the ferrite crystals.

3.4 Kinetics

The kinetics of the transformations in the Fe-C-Mo system were calculated three ways and are illustrated in Figs. 3.17, 3.18 and 3.19.

The first figure (3.17) plots the percentage of transformed ferrite as a function of time. This data was tabulated using a point counting method on micrographs 3.11(a) through 3.14(d). The growth rate is parabolic in shape.

Fig. 3.18 is a plot of thickness of ferrite on twin boundaries as a function of time. In this case the half thickness of the ferrite on the twins was measured and averaged for each transformation time. Again, the rate of thickening is a parabolic curve.

The last figure (3.19), plots the growth velocity as a function of transformation temperature (after Chatfield(51)) for Fe - 1%, .2/.4% C Mo alloys. This plot illustrates that the rate of growth is accelerated at high transformation temperatures but is retarded at lower temperatures.

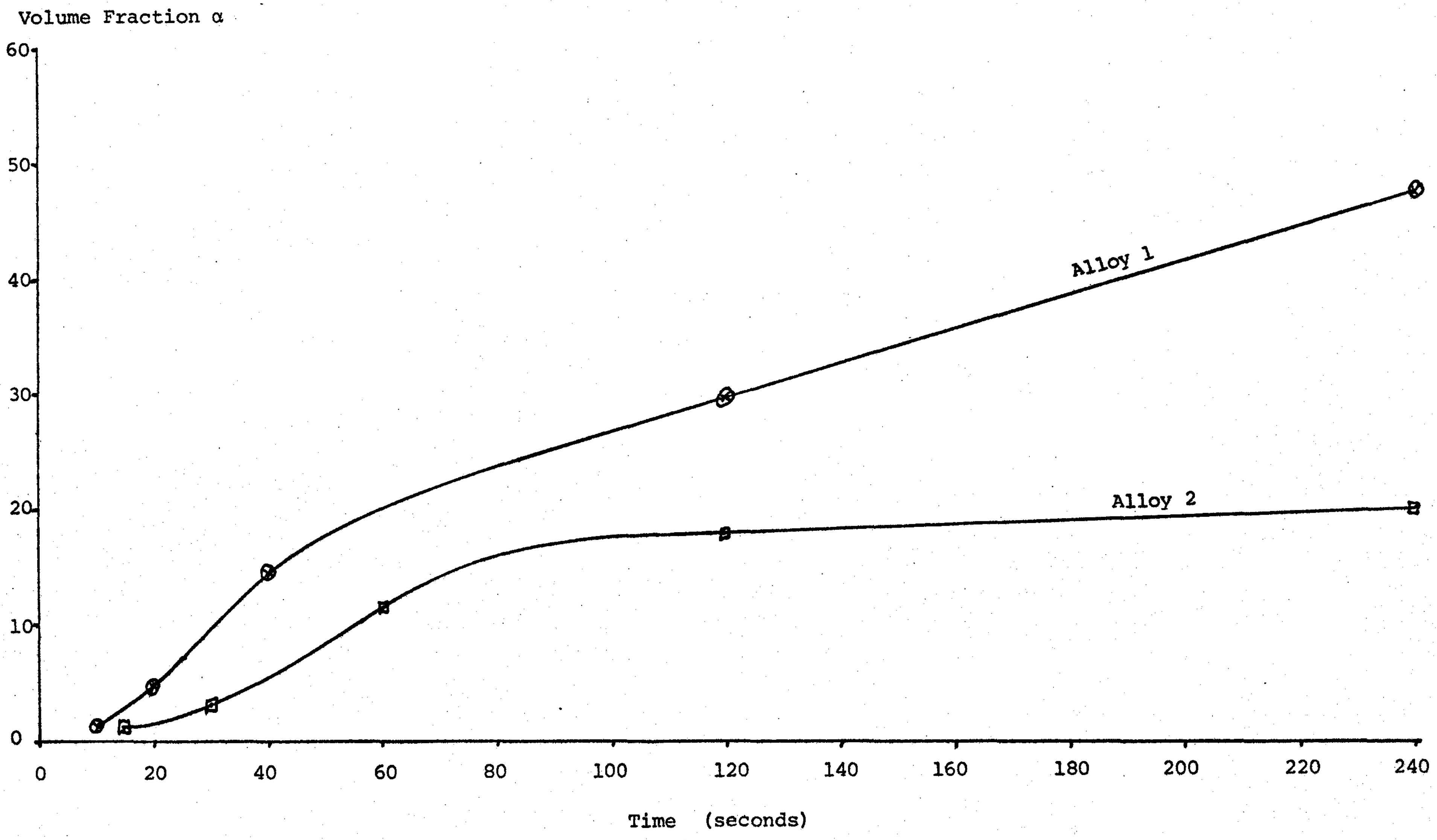

Figure 3.17(a) Volume fraction transformed as a function of time.

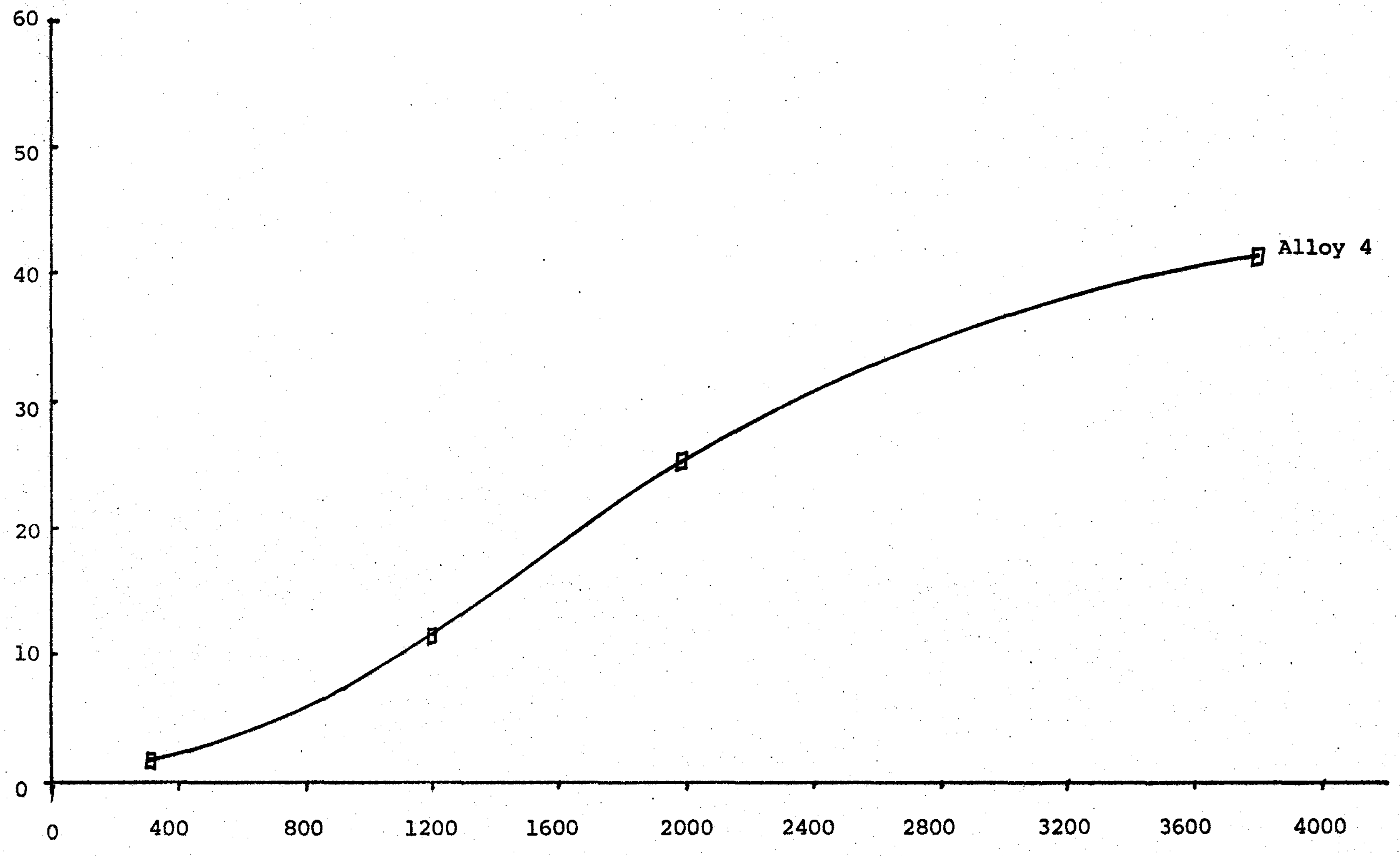

Time (seconds)

Figure 3.17(b) Volume fraction transformed as a function of time.

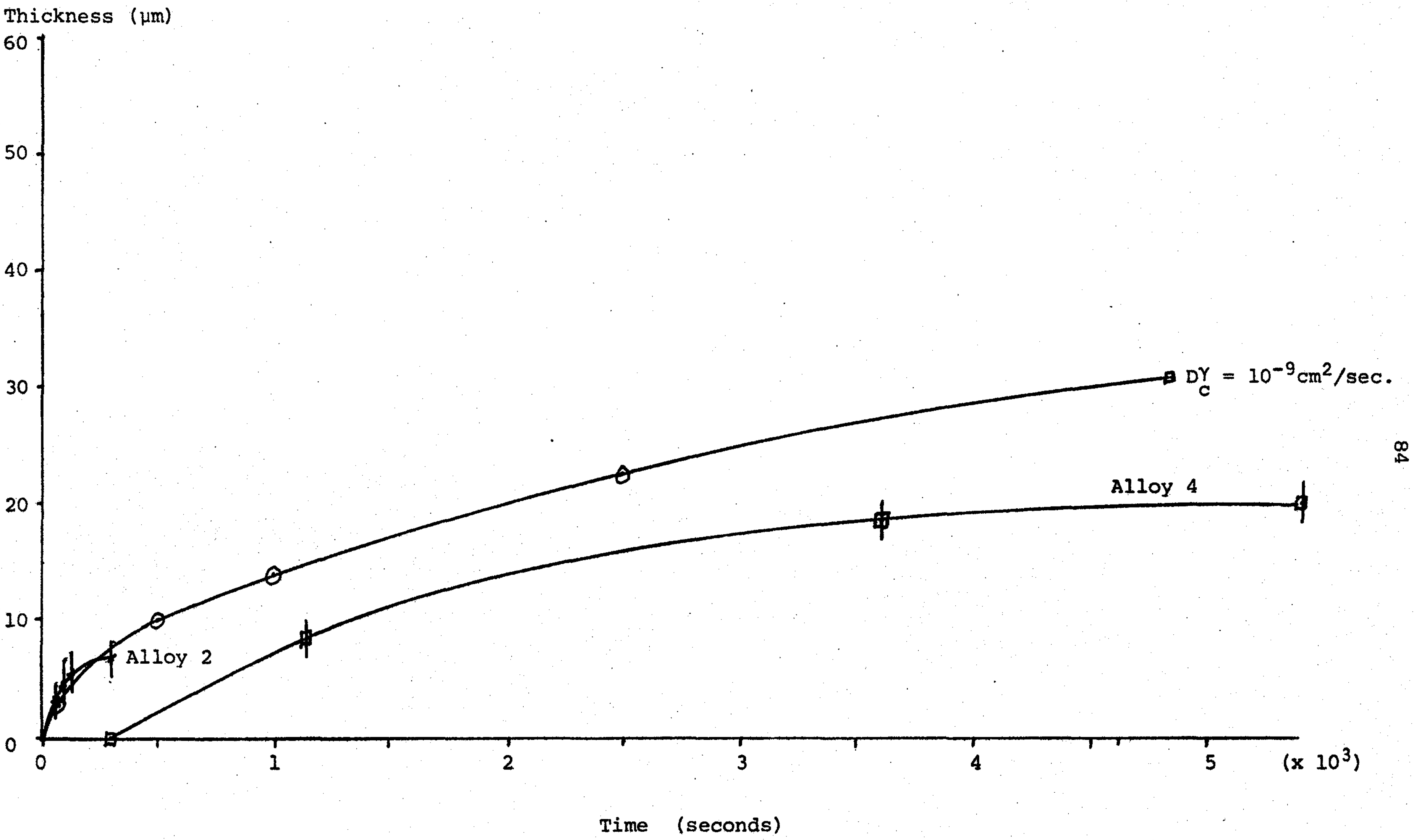

Figure 3.18 Half thickness of ferrite on twins as a function of time

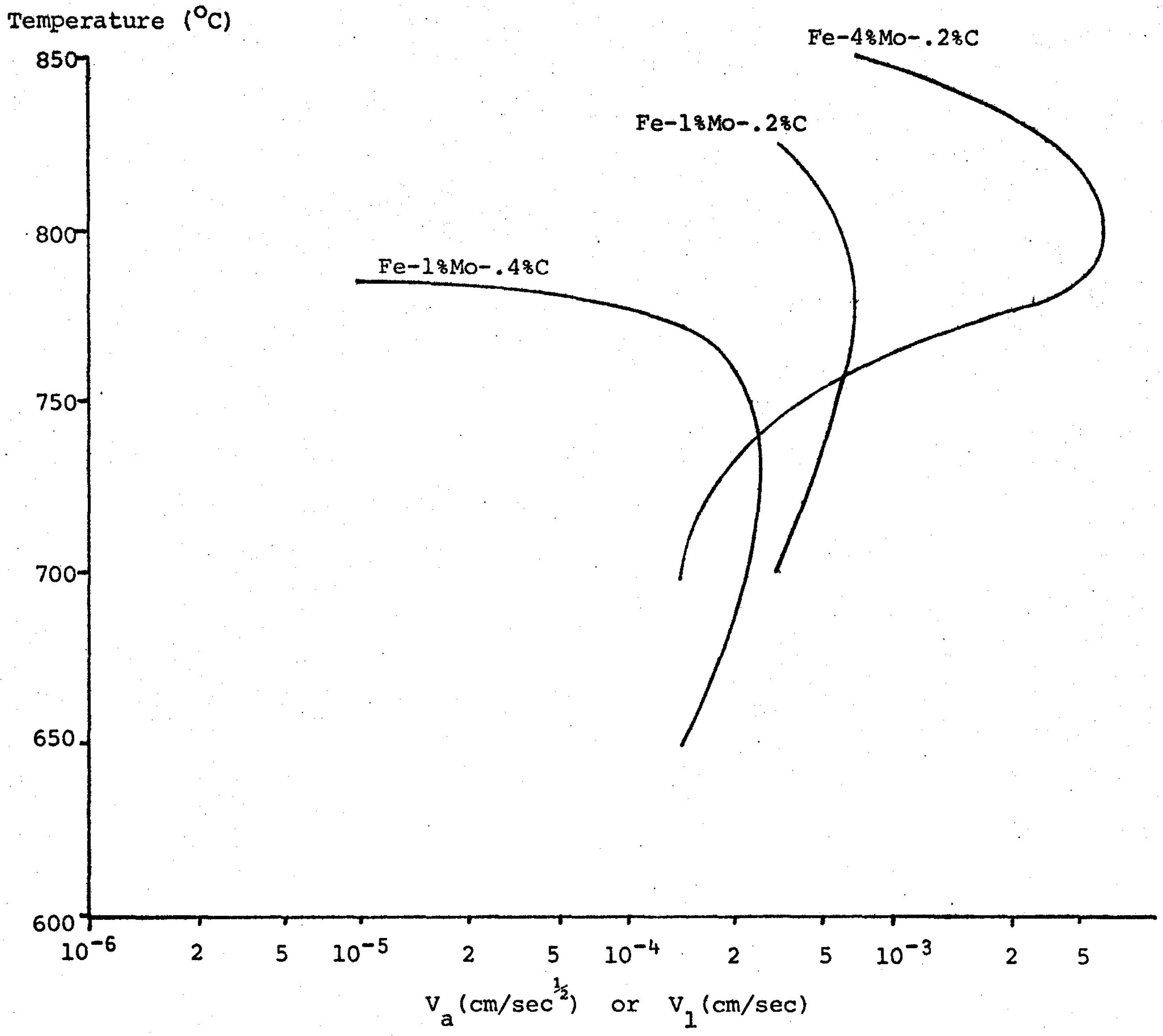

Figure 3.19 Growth velocity as a function of time (after Chatfield)

3.5 Mechanical Evaluation

Two types of tests were used to evaluate some of the mechanical properties of the four Fe-C-Mo alloys; these were microhardness and tensile tests.

The data obtained from the microhardness measurements is presented in Table 3.1. The measurements were made on alloys which had been transformed at 650°C for 150 minutes. The measurements were made on the proeutectoid transformation products, clean and wrinkled ferrite as well as the martensite which formed on quenching.

The lack of completeness of Table 3.1 is due to smallness of some of the features, i.e., accurate measurements could not be made in light of the indentor size and feature size.

In the higher carbon alloys 1838 and 1839 there are considerable differences in the hardness of the martensite compared to the wrinkled ferrite. However, in the lower carbon alloys there was only a marginal difference between the martensite and wrinkled ferrite. In all the alloys measured, the wrinkled ferrite was found to be harder than the clean ferrite.

The results of the tensile tests are presented in Fig. 3.20. The higher carbon alloys 3 and 4 fractured in the elastic region of the true stress vs. true strain curve. The fractures appear to be intergranular in nature. The lower carbon alloys 1 and 2 exhibited increasing ductility with decreasing carbon content. The .05 C alloy (1) had approximately 14% total elongation and the .18 C alloy (2) had 10%. The yield strength was 240 and 300 MPa for alloys 1 and 2 respectively. The ultimate tensile strengths are of the order of 520 and 610 MPa for alloys 1 and 2 respectively.

Table 3.1 Microhardness

Alloy	Clean Ferrite		Wrinkled Ferrite		Martensite	
	$\bar{X}$	S.D.	$\bar{X}$	S.D.	$\bar{X}$	S.D.
1	140.4	5.8	144.1	4.9		
2	157.8	21.5	187.9	8.2		
3			218.7	13.0	686.4	28.3
4			196.3	12.4	694.3	91.9

$\bar{X}$ - Mean S.D. - Standard Deviation

Notes:

1) All measurements are with a diamond Pyramid indenter.

2) Alloys 1, 2 and 3, 4 had insufficient martensite and clean ferrite, respectively, to obtain valid measurements.

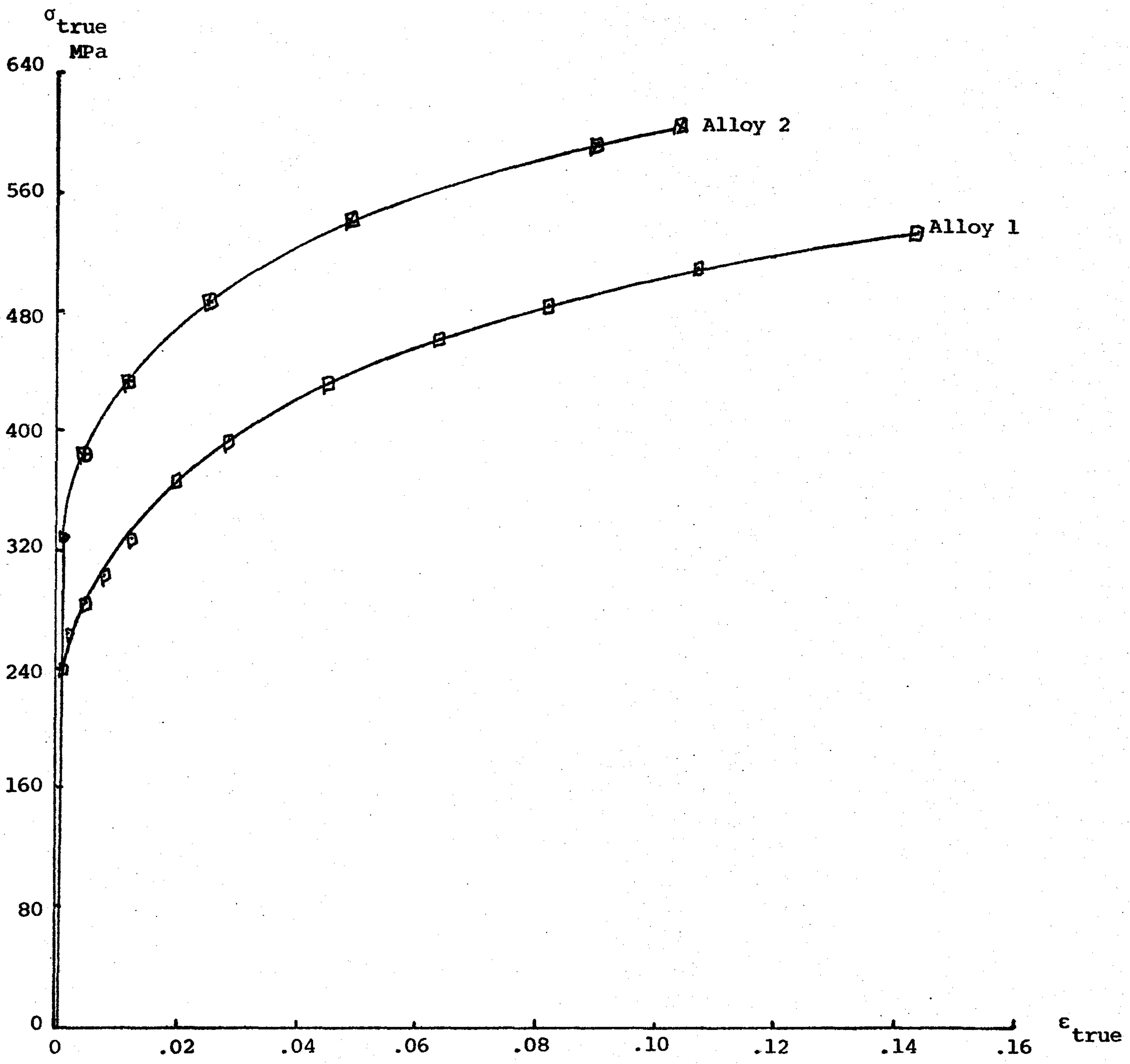

Figure 3.20 True Stress vs True Strain

CHAPTER 4

DISCUSSION

4.1 Continuous Cooling

Of the four Fe-C-Mo alloys, 3 (.28%C) and 4 (.43%C) produced a series of easily classified microstructural features over the length of the bar. The gradient of microhardness along the bar complemented the optical microstructures.

The microstructures originated as a martensitic structure with a microhardness of 426 and 653 DPH for alloys 3 and 4, respectively. With increased distance from the quenched end the structures progressed with decreasing hardness. These structures and hardness values are what one would expect from this type of cooling of a plain carbon steel but with a different distribution over the length and less Widmanstätten ferrite.

The two low carbon alloys 2 (.18%C) and particularly 1 (.05%C) produced morphologies which were much more difficult to classify. The range of hardness in these alloys is also correspondingly narrow, making the morphological classification even more difficult. The point of interest which arises in light of these observations is the difference between low carbon martensite and Widmanstätten ferrite. In terms of morphologies both structures are needle-like, with the martensite being a tetragonal supersaturated solution of carbon in α-iron and the Widmanstätten structure being cubic ferrite with carbon distributed as carbides inside or outside the ferrite laths. The range of hardness between these structures has been found to be very narrow, approximately 330 to 200 DPH for the martensite and Widmanstätten structures, respectively. In the hope of distinguishing these two microstructures, alloy 1 (.05%C) was tempered at a low temperature for one hour. The result was no change in the etching characteristics or morphology as seen in the optical mircoscope. The conclusion which can be drawn from these observations is that there is no specific depth at which the martensite clearly changes to a Widmanstätten structure or at which changes in carbide distribution can be identified in the Widmanstätten structures and that the optical morphologies of these structures are very similar.

4.2 Isothermally Transformed Structures

The first area to be dealt with is the formation of the substructure in the proeutectoid ferrite transformation product. Pitsch and Schrader(37) and Purdy(40) have shown that the wrinkled appearance of the proeutectoid product is a result of a very high dislocation density, similar to that found in a heavily cold-worked material, the order of 10^{12} cm^{-1}.

The nature of the substructure, i.e., the dislocation density, is well documented by these previous workers, but the origin of the substructure is still uncertain. As a consequence of some results from this work and results by Purdy, the following description of substructure formation is proposed.

The proeutectoid transformation product appears wrinkled, or heavily dislocated, when the transformation interface is less than optimally coherent. As coherency decreases across the transformation interface, more dislocations are required to assist in the lattice matching across the interface. The transformation interface is hence a possible source of the dislocations which form the substructure in the proeutectoid product. Work by Bäro and Perepezko(41) on Al-Ag alloys has shown that dislocations can be generated (up to very high densities, i.e., 10^{12} cm^{-1}) and absorbed by the transformation interface.

The next question to be considered is: How are the dislocations removed from the transformation interface? In Fig. 3.10 an optical micrograph was presented which illustrated the phenomena of interfacial precipitation. This was also shown by Purdy(40) (Fig. 3.9). In the electron micrograph of Purdy some additional contrast can also be observed in the austenite matrix. This observation in conjunction with the results of Honeycombe(35) indicates that some intracrystalline precipitation occurs in front of the transformation interface in the austenite matrix. These phenomena, interfacial and intracrystalline precipitation, are necessary processes for the proposed mechanism of substructure formation.

Consider Fig. 4.1(a); at the onset of the transformation, the carbide phases exist as interfacial and/or dispersed precipitates in the austenite. As the transformation progresses, the interface moves through the array of precipitates and dislocations are pulled out of the boundary by the precipitates to relieve coherency strains within the proeutectoid product phase. Some clean ferrite is also found to be formed, the controlling factor being the type of transformation interface, i.e., coherent, semi-coherent, or coherent, which will give an indication of its mobility and of the structure, i.e., many or few disclocations to account of lattice mismatch. In Fig. 4.1(c) the transformation interface has moved through the precipitate array leaving the highly dislocated proeutectoid phase. Purdy found that very fine carbides were attached to these dislocations. The present work, using extraction replication, these carbides

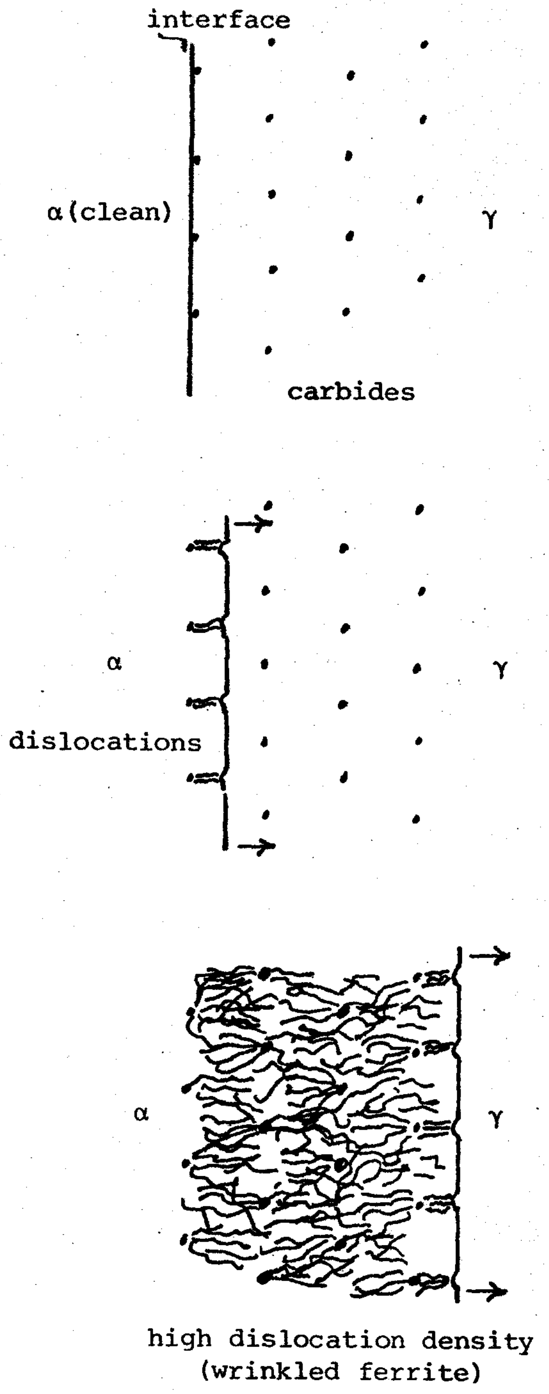

Figure 4.1(a)

Figure 4.1(b)

Figure 4.1(c)

Fig. 4.1 Schematic illustration of a migrating interface interacting with precipitates to form the wrinkled ferrite.

were not found, but were probably lost in the initial etching of the sample, even though the etching was very light. The carbides on the dislocations observed in the in-situ transformation observations (of Purdy(46)) therefore suggest that the precipitates dragged dislocations out of interface as it migrated.

The next question to consider, in light of this high dislocation density in the product phase, is: Where does the transformation interface get enough dislocations to produce the density which is found in the product phase and what is the effect on the interface when large numbers of defects are removed from it? A possible solution is that the dislocations which are dragged out of the interface come out as pairs with positive and negative Burgers vectors. Subsequent interaction between the dislocations from different pairs could result in complex tangles (which are common). If the dislocation pairs are of equal and opposite Burgers vector there would be no net decrease in the number of dislocations in the interface and the nature of the interface would be preserved. It is also possible for the free surface to act as a possible defect source, with the dislocations moving along grain boundaries from the surface to the transformation interface. The flow of dislocations could maintain a constant number of defects in the interface and hence the nature of the interface should not be altered.

The problem of dislocation generation is similar to the inverse in recrystallization. Here the question is: How can the interface mop up all those dislocations and retain its character?

4.3 Stability and the Equilibrium Shape

When the isothermally transformed alloys were reheated to a higher temperature within the two-phase region two observations were made.

First, the ferrite appeared as intragranular needles and second, it was not wrinkled ferrite, i.e., it did not exhibit the high dislocation density as indicated by the varied etching contrast.

The formation of clean intragranular ferrite after the second heat treatment indicates that clean ferrite is the more stable phase, as expected. The surprising feature of these results is the absence of grain boundary precipitates after equilibration. This is attributed to the resistance of the transformation induced substructure to recrystallization. The micrograph Fig. 3.15 indicated that the wrinkled ferrite has dissolved leaving only a "ghost" (carbides) on the grain boundaries. The new ferrite is then restricted to intragranular locations because the grain boundaries are covered with dislocated ferrite.

The resistance to recrystallization is undoubtedly related to the presence of carbides on the dislocations.

The needle shape which results from this coarsening process is probably due to surface energy minimization. The ferrite will be K - S related to the parent austenite grain. The driving force for growth is such that the system will be very close to equilibrium at all times.

Hence it seems reasonable to assume that the intragranular needles are K - S related to the austenite and the aspect ratio is such that the interfacial energy is minimized, i.e., we have a measure of the equilibrium shape aspect ratio, which is approximately 24 to 1.

The growth of clean ferrite at the expense of the wrinkled ferrite provides an additional energy contribution for coarsening, the reduction in dislocation density. The energy of a dislocation is proportional to the square of the Burgers vector; if this is assumed to be constant in both forms of ferrite, then the difference in energy will be a function of the length. Hull$^{(54)}$ has stated that the elastic strain energy of a dislocation is the order of 4×10^{-4} ergs/cm. Based on the reduction of dislocation density from 10^{12} to 10^{6} cm^{-1}, the energy contribution will be of the order of 70 cal/mole compared to a typical stored energy of approximately 20 to 200 cal/mole for a plastically deformed material.

4.4 Ferrite Growth on Twins

The nucleation of ferrite in plain carbon steels generally occurs heterogeneously. Consider the nucleation of an α crystal in γ. If the α nucleates on a grain boundary the surface energy barrier to nucleation is reduced because grain boundary area is eliminated and a new $\alpha\gamma$ interface is created. Here the free energy barrier is:

$$\Delta G(d) = ad^2(\Delta G_V + \Delta G_\varepsilon) + bd^2\gamma_{\alpha\gamma} - cd^2\gamma_{\gamma\gamma}$$

where d is the maximum dimension of any nucleus and a, b and c are constants which depend on the ratio of $\gamma_{\gamma\gamma}/\gamma_{\alpha\gamma}$ (after Shewmon$^{(47)}$).

This treatment provides a method of understanding the nucleation of ferrite on twins in Mo steels, the comparison of the twin boundary energy to the interfacial energy of the nucleus and the matrix.

A twin boundary provides a unique substrate for nucleation since the twinning plane (111) is a plane of mirror symmetry. A K - S related ferrite crystal can therefore extend into both austenite crystals, remain K - S related to each and not contain any boundary. This is because the high symmetry (110) plane in ferrite is parallel to the (111) in austenite and is shown in Fig. 4.2.

Nucleation models based on classical nucleation theory require a shape for the critical nucleus and values for surface energies. Several models for the shape of the critical nucleus have been proposed$^{(48,49)}$ and surface energies have been calculated where possible.

The model for the critical nucleus developed in this work is based

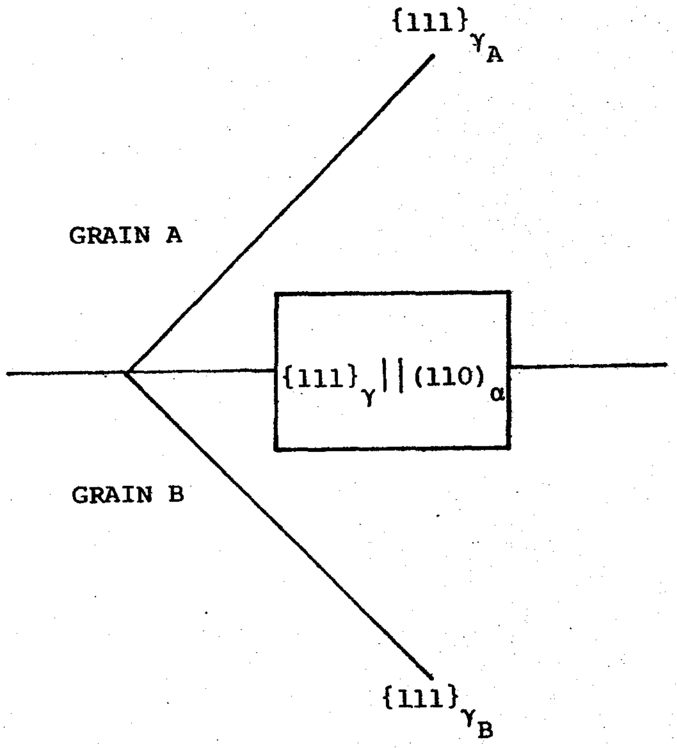

Fig. 4.2 A twin boundary in austenite and a ferrite nucleus, illustrating the high symmetry (110) plane in α parallel to the (111) in γ.

on the energy balance criterion described by Cahn and Hoffman$^{(29)}$. Their model was based on two isotropic spherical caps as in Fig. 4.3(a) but the energy balance described is applicable to anisotropic shapes. The shape of the critical nucleus was developed by determining the energies of different interfaces (incoherent, semi-coherent and coherent) and using these values in the equations to calculate nucleation rates and times based on classical theory. The symmetry of the nucleation substrate was an important boundary condition.

The twin boundaries provide a mirror plane for the K - S related ferrite as well as the austenite. The energy of this boundary has been determined by Dunn et al.$^{(50)}$ and is approximately 190 ergs/cm^2. The Cahn-Hoffman construction contains the energy balance for isotropic or anisotropic systems and determines θ, the contact angle as illustrated in Fig. 4.3 (a). No attempt is made to determine a value for θ in this work. However, by setting $\theta = 0°$ a limiting condition solution is available which will predict a shape which is applicable over a range of contact angles, 0° through 90°. For $\theta = 0°$, this is the condition for spontaneous nucleation and complete wetting of the grain boundaries. The condition is illustrated in Fig. 4.3 (b) for a double hemispherical cap nucleus (i.e., an isotropic system).

The energy balance is shown in Eq. 4.1:

$$\gamma_T = 2\gamma_{\alpha\gamma} \cos \theta \qquad (4.1)$$

and for the condition $\theta = 0°$:

$$\gamma_T = 2\gamma_{\alpha\gamma} \qquad (4.2)$$

hence the minimum value of α/γ interface is 95 ergs/cm^2. The interface being considered is a coherent boundary (low energy) which previous investigators had given a value of 30 ergs/cm^2. However, if this value

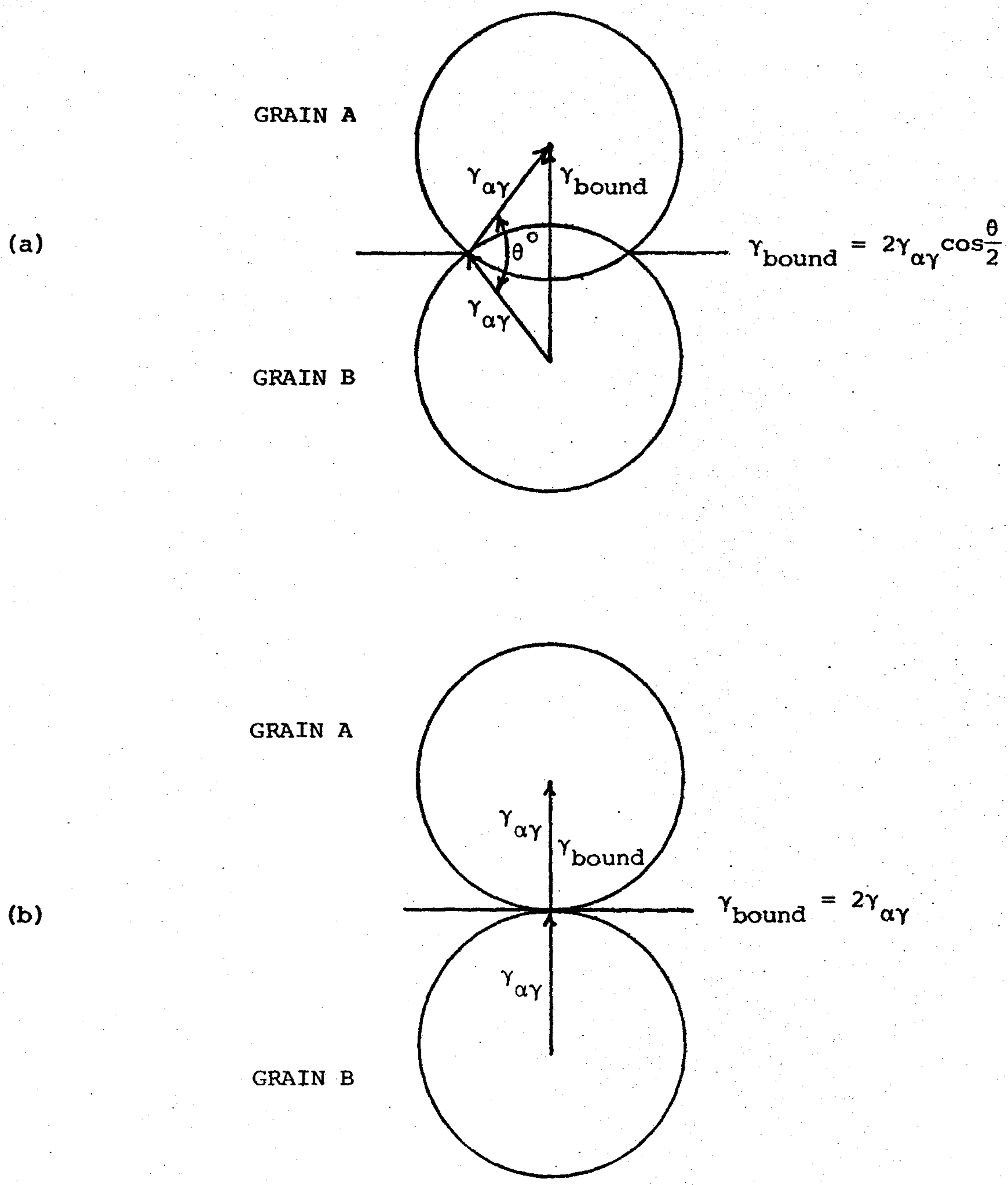

Fig. 4.3 (a) Nucleation model of Cahn and Hoffman based on two isotropic spherical caps.
(b) Condition for spontaneous nucleation, i.e., θ=0°.

of $\gamma_{\alpha\gamma}$ is substituted into Eq. 4.2, an imbalance exists and nucleation would occur spontaneously on all twins. Hence, the existence of high energy twins (190 ergs/cm^2) is enough to eliminate the low energy α/γ interface.

The value calculated for the α/γ interface when substituted into classical rate and time equations (Appendix 1) predicts times of the order of 10^6 years based on the existing configuration of the classical nucleus. To produce reasonable nucleation rates and retain classical nucleation theory the size and shape of the critical nucleus must be reassessed. The model proposed by Sharma and Purdy(48) was a disc shape (Fig. 4.4(a)) corresponding to the double hemispherical cap, adapted for anisotropy). This shape was also used by Morral and Cameron(49). Their arrangement of nuclei was not symmetrical as they were using a grain boundary as the nucleation substrate, with the ferrite having one coherent and one incoherent interface with the austenite.

As a result of the higher energy for the coherent interface inferred here, a reduction is required in both surface and volume free energy for the critical nucleus. This was accomplished by truncating the sides of the disc (Fig. 4.4(b)). As well as reducing the volume some of the high energy interface is replaced by a lower energy boundary. Also inherent in this new shape is the symmetry which is known to exist around a twin boundary. Substituting the new distribution of surface energy and the reduced volume term into the classical equations predicts reasonable kinetics within the bounds of classical nucleation theory.

The configuration of the critical nucleus can also be used to model nucleation of Widmanstätten side plates, when rotated perpendicular to the interface (Fig. 4.5(a)). In this case the planar low energy faces of

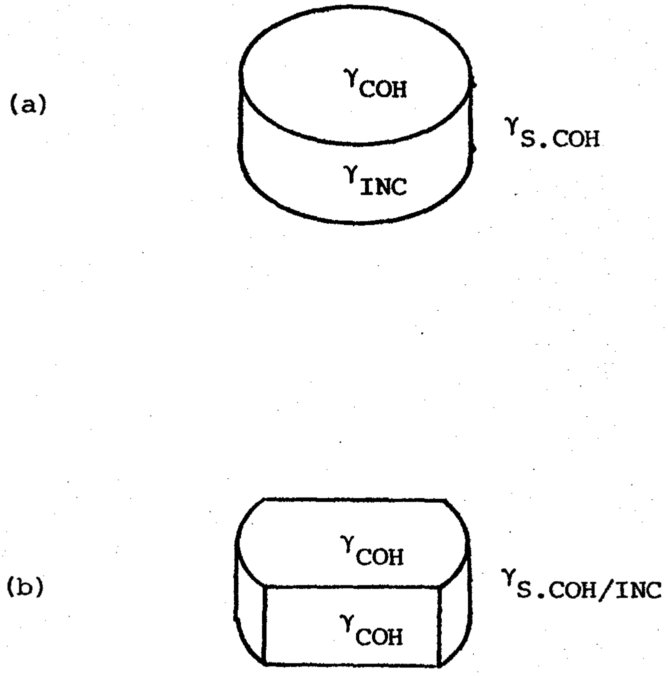

Fig. 4.4 (a) Disc shape critical nucleus proposed by Sharma and Purdy.(48)
(b) Truncated disc critical nucleus proposed here.

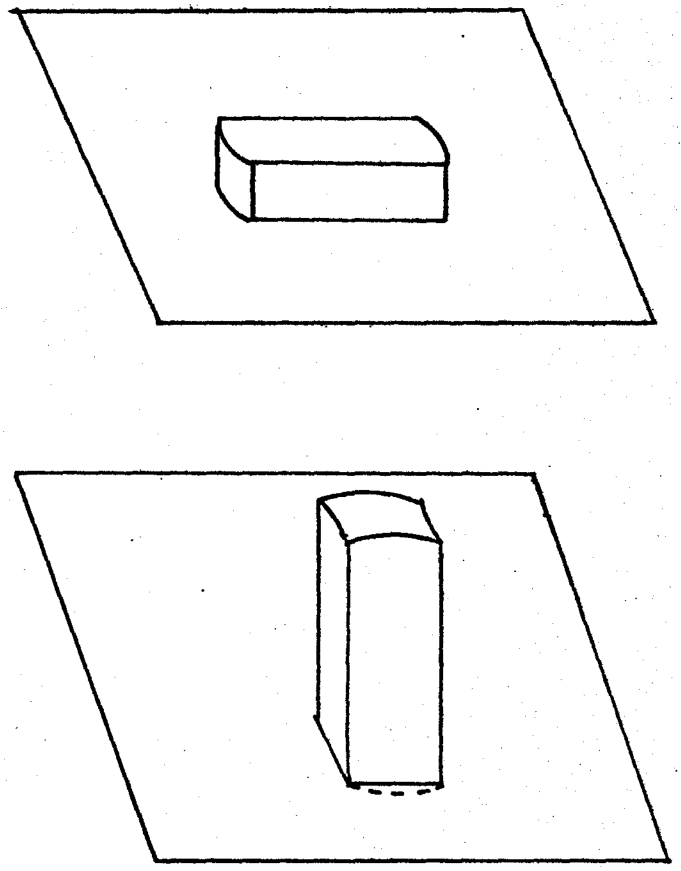

Fig. 4.5 Two variations illustrating the application of the truncated disc critical nucleus to Widmanstätten nucleation.

the truncated disc corresponds to the planar coherent faces of the needle and the high energy incoherent end of the truncated disc corresponds to the growing tip of the needle, which is incoherent with respect to the matrix.

The truncated disc as presented as a model for the critical nucleus satisfies all the boundary conditions that it has been subject to, as well as providing a model for Widmanstätten nucleation. Based on this, the truncated disc is a reasonable configuration for the critical nucleus. However, alternative configurations are also possible if they can satisfy the limiting conditions which have been determined here. A variation of the Widmanstätten orientation is shown in Fig. 4.5(b) with the needle in the plane as opposed to a perpendicular orientation.

The application of the needle shape to grain boundary nucleation is straightforward, as shown in Fig. 4.5. Note that the equilibrium shape inferred in Section 4.3 is consistent with this model.

4.5 Kinetics of Ferrite Growth

The growth kinetics of the proeutectoid ferrite can be described as parabolic according to Figs. 3.17 and 3.18. The calculated rate of carbon diffusion (Appendix 2) is plotted on the same figures and is approximately equal to the growth rates.

These results are somewhat confusing in light of Fig. 4.6 which schematically illustrates that increasing the amount of Mo in the alloy increases the rate of growth at high temperatures (750°C) but retards growth at lower transformation temperatures (650°C). The transformations and kinetic measurements were made at 650°C, which according to Fig. 4.6 should yield kinetics which are somewhat retarded, and therefore not determined by the rate of bulk carbon diffusion in α-iron.

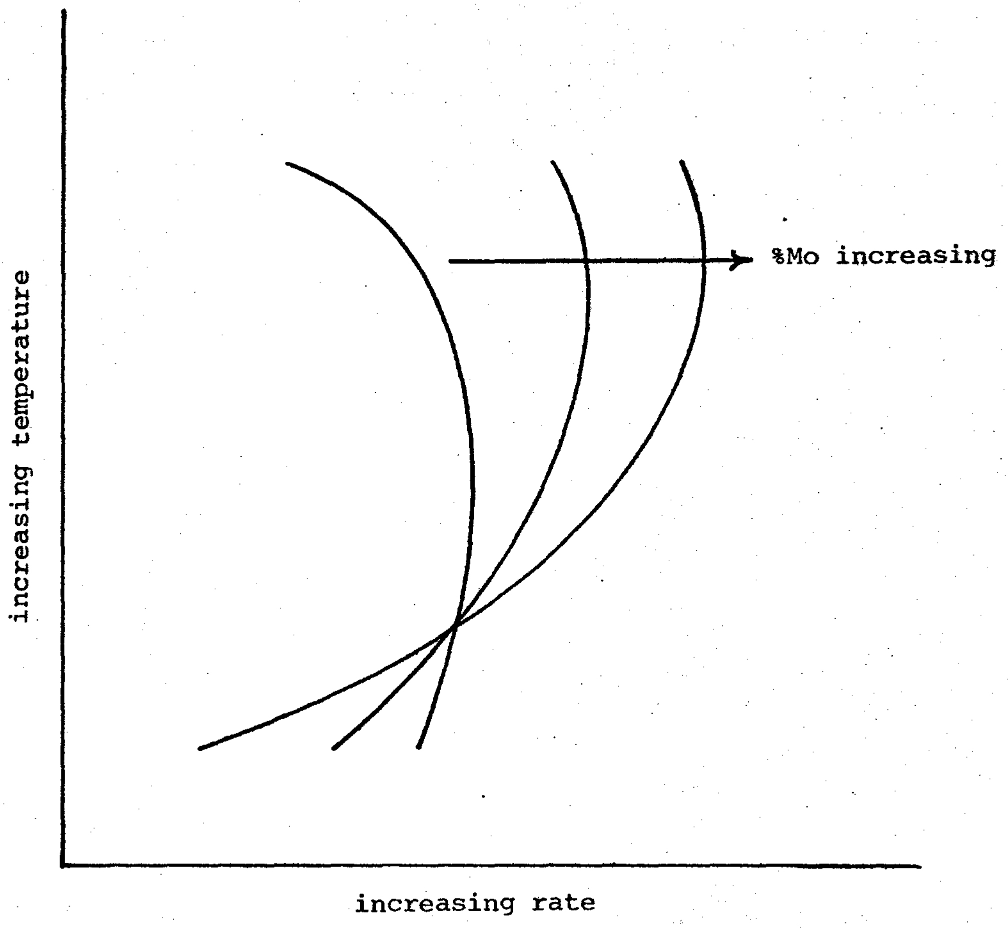

Fig. 4.6 Schematic illustration of the effect of Mo on transformation kinetics.

We will now consider how interfacial precipitation might effect ferrite growth. Using an approach similar to that of Purdy, Weichert and Kirkaldy(34), i.e., extending the local equilibrium model to a ternary system in which the two solutes, C and Mo, for this case, diffuse at vastly different rates.

If an isothermal section of the Fe-C-Mo phase diagram is considered, Fig. 4.7(a) the effect of Mo additions at constant C is to increase the supersaturation. If the 1wt.% Mo line is labelled A, the precipitation of Mo_2C will shift this tie line towards the equilibrium solubility, labelled B. The net effect of this precipitation process is therefore to decrease both the Mo and C at the interface which results in a net decrease in the supersaturation. This is now a pseudobinary problem and can be considered as illustrated in Fig. 4.7(b). Prior to the precipitation of Mo_2C the carbon potentials are given as C_α, C_γ and C_0 for the ferrite, austenite and bulk phases, respectively. The precipitation of Mo_2C lowers the carbon potential in the austenite at the interface to C_γ', illustrated in Fig. 4.7(b). This carbon potential can be evaluated by taking the carbon isoactivity line from the point C to the intersection with line A. This point now determines the new carbon potential C_γ' at the interface after precipitation.

The reduction in supersaturation $\Delta C = C_\gamma - C_\gamma'$ is proportional to ΔMo. The effect of decreasing the supersaturation is to lower the driving force for diffusional growth, hence at lower temperatures, where precipitation of Mo_2C is observed, the rate of growth is decreased but may still be carbon diffusion controlled. This model provides a reasonable explanation for the retarded but parabolic and apparently carbon diffusion controlled kinetics at the transformation temperature of 650°C. Experi-

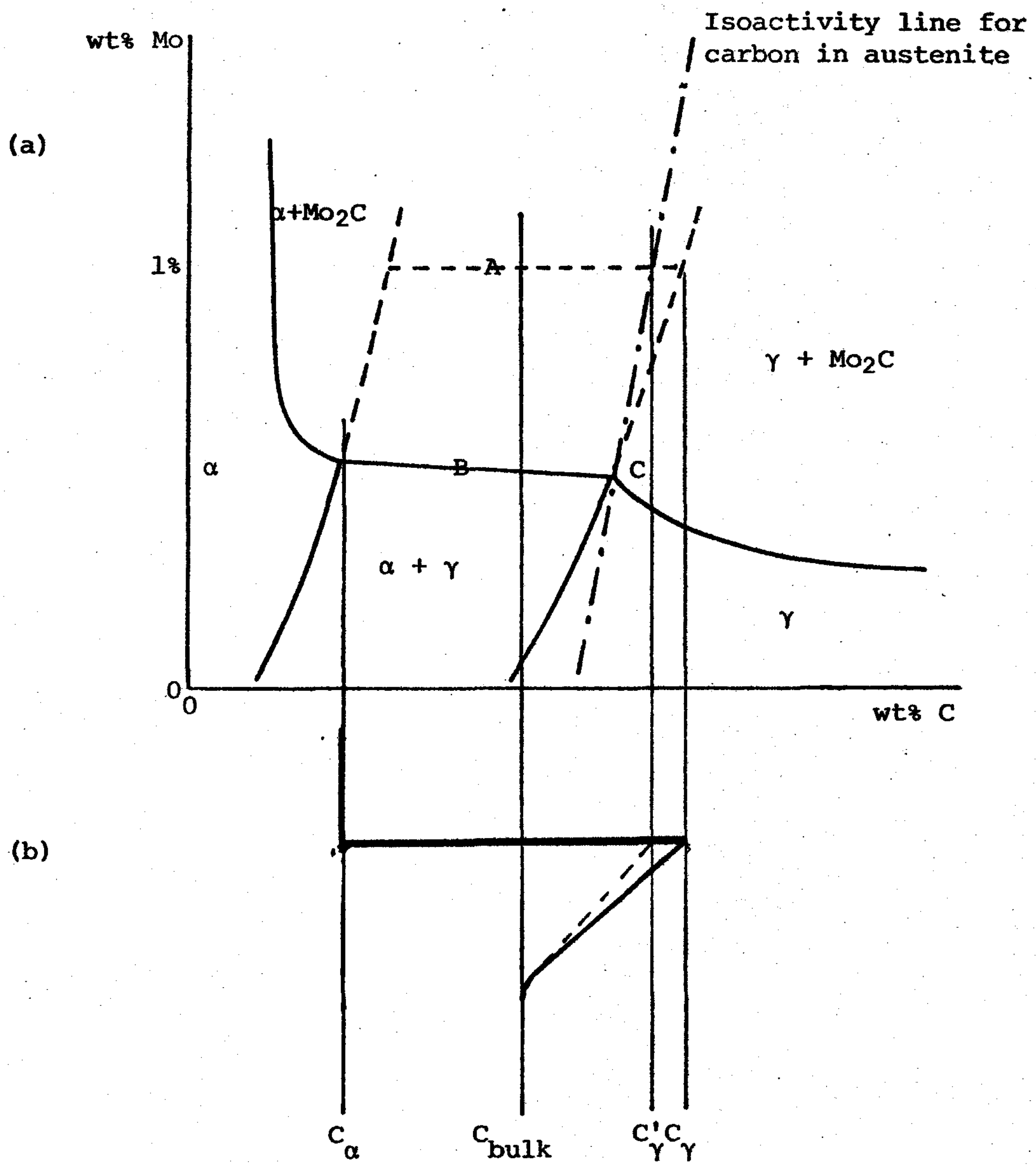

Fig. 4.7 (a) Approximate isothermal section of the Fe-C-Mo system @ 800°C.
(b) Pseudobinary approximation of interfacial carbon potential.

mental observation using transmission electron microscopy and the electron microprobe has shown that these precipitates and precipitation processes occur at these temperatures.

However, in choosing to carry out the transformations at 650°C, the deepest portion of the bay in the TTT curves was missed; it occurs in the 600°C temperature range. Hall, Kinsman and Aaronson(52) found that the growth of proeutectoid ferrite was first "clean" and after some time the precipitation of Mo_2C occurred. In the deepest portion of the bay it would be possible to have more than the reduction of carbon supersaturation acting to retard the growth process. Precipitates acting to slow down the migrating interface by acting as obstacles to interface motion could further retard the transformation rates.

Kinsman and Aaronson(45) described a theory known as impurity drag effect which they felt to be the cause of the retardation in the kinetics. The basis of the theory is that solute adsorbed by the migrating interface would cause it to slow down. However, it is felt that the effect of decreased supersaturation and the interaction of precipitates with the migrating interface provide a good corelation with the measured kinetics.

4.6 Mechanical Behavior

The high dislocation density found in the wrinkled ferrite, the order of 10^{12} cm/cm^3, gives mechanical behavior similar to that of a cold worked material. The mechanical behavior was very much dependent on the grain size; this was observed by changes in the time and temperature of austenitization.

The two high carbon alloys 3 (.28%C) and 4 (.43%C) fractured before the yield stress was reached. The dislocation tangles would not permit sufficient movement to accommodate slip. This indicates that the dislocation tangles are immobile and that the material fractures in a brittle nature (also supported by the appearance of the fracture surface).

The low carbon alloys 1 (.05%C) and 2 (.18%C) exhibited both yield and ultimate tensile stresses. Increasing ductility was also observed with decreasing carbon content. This behavior indicates that carbon content and hence carbide precipitates have a role in determining the mechanical response of these alloys. The higher carbon alloys whose early failure, attributed to immobile dislocations, could be pinned by carbides. In light of observations showing carbides attached to dislocations and the mechanism by which dislocations are removed from the boundary make this seem a logical conclusion. In lowering the carbon content, the amount of precipitation is reduced and dislocation movement is less restricted, giving rise to the properties exhibited by the lower carbon alloys.

CHAPTER 5

CONCLUSIONS

As a result of the investigation of the effect of Mo on the proeutectoid ferrite reaction in steel, the following conclusions can be made:

1. Experiments show evidence for both interfacial and intracrystalline precipitation.
2. Growth kinetics - thickening of grain boundary precipitates are parabolic and determined approximately by the rate of carbon diffusion in austenite.
3. The retardation of growth kinetics at intermediate reaction temperatures is postulated to be due to decreased supersaturation caused by the precipitation of carbides (Mo_2C) at these temperatures.
4. If classical nucleation theory is to describe ferrite nucleation from austenite the shape of the critical nucleus must be altered to the model proposed here.
5. The equilibrium shape in the Fe-C-1%Mo system is a needle.
6. The substructure is stabilized by precipitation to the extent that recrystallization does not occur even when the ferrite is heated above 750°C.

APPENDIX 1

The nucleation rate (J) as calculated by Sharma and Purdy$^{(35)}$ based on the disc shape critical nucleus and γ_{coherent} = 30 ergs/cm^2 was greater than 10^{15} nuclei/cm^2 sec. Using the value of γ_{coherent} (95 ergs/cm^2) determined in this work, a ratio was determined:

$$\frac{J_{30}}{J_{95}} = \frac{\frac{2\pi D}{a^4}\, r^{*2}_{30}\, \bar{C}\,(1\text{-}\cos\,\theta)\, \frac{N_o}{C}\, \exp(-\Delta G^*_{30}/kT)}{\frac{2\pi D}{a^4}\, r^{*2}_{95}\, \bar{C}\,(1\text{-}\cos\,\theta)\, \frac{N_o}{C}\, \exp(-\Delta G^*_{95}/kT)}$$

$$= \frac{\exp(-\Delta G^*_{30}/kT)}{\exp(-\Delta G^*_{95}/kT)}$$

where $\Delta G^* \; \alpha \; \gamma_{\text{semicoherent}}{}^2 \gamma_{\text{coherent}}/\Delta G_v{}^2$

$$\therefore \; \frac{J_{30}}{J_{95}} = k \, \exp\left[[\frac{\gamma_{SC}{}^2\gamma_{95} - \gamma_{SC}{}^2\gamma_{30}}{\Delta G_v}]/kT \right]$$

$$= \infty$$

Hence, nucleation should not occur according to this model with γ_{coherent} = 95 ergs/cm^2.

By increasing the γ_{coherent}, the critical volume is increased by a corresponding factor according to

$$V^* = -2\gamma_{SC}{}^2 \; \gamma_C/\Delta G_v \qquad (35)$$

Hence, by truncating the disc critical nucleus, the volume can be reduced to the original volume. By replacing high energy interface with lower energy (95 ergs/cm^2) interfaces, the rates calculated by Sharma and Purdy, i.e., J = 10^{15} nuclei/cm^{2}sec., will be the rate.

APPENDIX 2

Calculation of diffusion rates of carbon in austenite.

$$D_C^{\gamma} = D_0\{\chi\} \exp\,[-\,Q_D\{\chi\}/RT] \;\; \mathrm{cm}^2/\mathrm{sec}$$ (after Wells et al.(53))

where $D_0\{\chi\} \approx 0.5 \exp\,[-\,30\,\chi] \;\; \mathrm{cm}^2/\mathrm{sec}$

and $Q_D = 38{,}300 - 1.9 \times 10^5\chi + 5.5 \times 10^5\chi^2$ cal/mole

Hence
$$D_C^{\gamma}(\chi) = 0.5 \exp\{-\,30\,\chi\} \exp\left[\frac{-\,38{,}300 - 1.9 \times 10^5\chi + 5.5 \times 10^5\chi^2}{RT}\right]$$

T °C	C	D_C^{γ} cm²/sec
650	.0043	7.5×10^{-10}
650	.0018	4.9×10^{-10}

REFERENCES

1) Dubé, C.A., H.I. Aaronson and R.F. Mehl, Rev. Met. 55, (1958), p.201.

2) Heckel, R.W. and H.W. Paxton, Trans. ASM, 53, (1961), p.539.

3) Barrett, C.S., A.H. Geisler and R.F. Mehl, Trans. AIME, 143, (1941), p.134.

4) Carter, A.J., J. Inst. Metals, 83, (1955), p.481.

5) Aaronson, H.I., W.B. Triplett and G.M. Andes, Trans. AIME, 218, (1960), p.331.

6) Mehl, R.F. and O.T. Marzke, Trans. AIME, 93, (1931) p.123.

7) Newkirk, J.B., Ph.D. Thesis, Carnegie Inst. of Technology, (1950).

8) Aaronson, H.I., Decomposition of Austenite by Diffusional Processes, Interscience New York, (1963) p.391.

9) Manning, G.K. and C.H. Lorig, Trans. AIME, 167, (1946), p.442.

10) Shewmon, P.G., Transformations in Metals, McGraw Hill, (1969), p.159.

11) Mazanec, K. and J. Cadek, Rev. Met., 212, (1958), p.501.

12) Hickley, C.M. and J.H. Woodhead, J. Iron and Steel Inst. (London), 176, (1954), p.129.

13) Zener, C., J. Appl. Phys., 20, (1949), p.950.

14) Bradley, J.R., J.M. Rigsbee and H.I. Aaronson, Met. Trans. 8A, (1977), p.323.

15) Townsend, P.D. and J.S. Kirkaldy, Trans. ASM, 61, (1968), p.605.

16) Kurdjmov, G.V. and G. Sacks, Z. Physik, 64, (1939), p.325.

17) Sekerka, R.F., J. Phys. Chem. Solids, 28, (1967), p.983.

18) Mehl, R.F. and C.S. Barrett, reply to discussion, ref. Mehl, R.F., C.S. Barrett and D.W. Smith, Trans. AIME, 105, (1953), p.215.

19) Nabarro, F.R.N., Proc. Phys. Soc. (London), 53, (1940), p.90.

20) Nabarro, F.R.N., Proc. Roy. Soc. (London), 175, (1940), p.519.

21) Jones, G.J. and R. Trivedi, J. Appl. Phys., 42, (197), p.42 9.

22) Laszlo, F., J. Iron and Steel Inst. (London), 147, (1943), p.173.

23) Ibid. 148, (1943), p.137.

24) Ibid. 150, (1944), p.183.

25) Ibid. 152, (1945), p.207.

26) Ibid. 164, (1950), p.5.

27) Smith, C.S., Trans. AIME, 137, (1940), p.313.

28) Kinsman, K.R., E. Eichen and H.I. Aaronson, Met. Trans. 6A, (1975), p.303.

29) Hoffman, D.W. and J.W. Cahn, Surface Science, 31, (1968) p.368.

30) Shewmon, P.G., Transformations in Metals, McGraw-Hill, (1969), p.245.

31) Purdy, G.R., Metallography, 7, (1975), p.131.

32) Coates, D.E., unpublished research

33) Li, C.Y., J.M. Blakley and A.H. Feingold, Acta Met., 14, (1966), p.1397.

34) Purdy, G.R., D.H. Weichert and J.S. Kirkaldy, Trans. AIME, 230, (1964), p.1025.

35) Honeycombe, R.W.K., Met. Trans. 7A, (1976), p.915.

36) Hultgren, A., Kungl. Svenska Velenskapskademiens Handlingar, Band 4, N:o 3, (1953).

37) Pitsch, W. and A. Schrader, unpublished research.

38) Berry, F.G., and R.W.K. Honeycombe, Met. Trans., 1, (1970), p.3279.

39) Ibid.

40) Purdy, G.R., Acta Met., 26, (1978), p.487.

41) Bäro, G. and J.H. Perepezko, Material Science and Engineering, 28, (1977), p.243.

42) Goldschmidt, H.J., Interstitial Alloys, Plenum Press, (1967), p.108.

43) Barbacki, A. and R.W.K. Honeycombe, Metallography, 9, (1976), p.277.

44) Rigsbee, J.M. and H.I. Aaronson, unpublished research.

45) Kinsman, K.R. and H.I. Aaronson, Transformation and Hardenability in Steels, Climax Symposium, (1967), p.39.

46) Purdy, G.R., private communication.

47) Shewmon, P.G., Transformations in Metals, McGraw-Hill, (1969), p.215.

48) Sharma, R.C. and G.R. Purdy, Met. Trans., 4, (1973), p.2303.

49) Morral, J.E. and T.B. Cameron, Met. Trans., 8A, (1977), p.1817.

50) Dunn, C.G., F.W. Daniels and M.J. Bolton, J. of Metals, (1958), p.368.

51) Chatfield, C., unpublished research.

52) Hall, M.G., K.R. Kinsman and H.I. Aaronson, J. Iron and Steel Inst., July, 1972, p.541.

53) Wells, Batz and R.F. Mehl, Trans. AIME, 188, (1950), p.533.

54) Hull, D., Introduction to Dislocations, Pergamon Press, 1975, p.92.